ESA Contract Report

ESA 4000130590/20/NL/IA

Contract Report to the European Space Agency

Final Report: Study to assess earth observation with small satellites and their prospects for future global numerical weather prediction

Final report for ESA contract no. 4000130590/20/NL/IA

Authors: Katie Lean, Niels Bormann, Sean Healy and Stephen English

October 2022

Series: ECMWF ESA Contract Report Series

A full list of ECMWF Publications can be found on our web site under:
http://www.ecmwf.int/en/publications/

Contact: library@ecmwf.int

Contents

1 Introduction **2**

2 Use of the Ensemble of Data Assimilations to assess observation impact **4**

2.1 Methodology of the EDA 4

2.2 Application of the EDA to simulate impact of future observations 5

2.3 EDA experimental set up 6

2.4 Relating EDA spread change to forecast error 6

3 Potential future constellations **10**

4 Framework for simulating and assimilating small satellite data **12**

4.1 Simulating MW brightness temperatures 13

4.2 Sampling and thinning 14

4.3 Adding noise to simulated observations 16

4.4 Observation error model adaptation 16

4.5 Realism of brightness temperatures 18

4.6 Assimilation 19

5 EDA spread results **20**

5.1 Observation distribution 23

5.2 Sensitivity to thinning 25

6 Conclusions and further work **26**

A Considerations for 3x3 averaging **30**

B Outline of the all sky observation error model **30**

C Estimation of small satellite clear sky observation errors **35**

Abstract

Small satellites are expected to become an important component of the future observing system and will complement a continued backbone of larger, high-performance platforms. An Ensemble of Data Assimilations (EDA) method is employed to evaluate the impact of different potential future small satellite constellations carrying MW sounding instruments to explore the optimal design of a constellation for global Numerical Weather Prediction (NWP). Six different potential constellations of small satellites are chosen to probe key aspects of the constellation design: the number of satellites, types of orbits and the trade-off between having 183-GHz humidity sounding channels (complemented with window channels at 89-and 165-GHz) or with additional temperature sounding capability in the 50-GHz band. The small satellite data and accompanying observation errors are simulated, using an all-sky framework, and the benefit from adding the data to the observing system is measured by reducing the spread of the ensemble members which reflects improvement to the uncertainties in analyses and forecasts.

The reduction in EDA spread for different variables (e.g. wind and geopotential height) and pressure levels is already significant using a smaller constellation of eight satellites added to a 4-satellite baseline. The EDA spread reduction continues as further observations are added although the rate of reduction slows, especially where scenarios only include use of humidity sounding channels. The use of temperature sounding channels gives a significant added benefit over humidity sounding only generally in the order 2-3 and 1.5-2 times larger in the extra-tropics and tropics respectively. Different behaviour in the relative magnitudes and rates of EDA spread reduction is seen generally between the extra-tropics and tropics which can be attributed to different physical processes and different spatial and temporal growth of errors in the EDA. Advantages of using small satellites in polar orbits only, mid-inclination orbits only or a mix of orbits are difficult to distinguish especially due to a suboptimal interaction between the chosen satellite phasing and current thinning strategies.

1 Introduction

Observations from microwave (MW) instruments currently provide the greatest impact of the satellite data used in the ECMWF assimilation system (Bormann et al., 2019). We presently benefit from a good number of MW instruments with temperature and humidity sounding capabilities from a variety of polar orbiting platforms, not least since many sensors are operating well beyond their design life. Duncan et al. (2021) demonstrated the significant benefit of adding existing MW temperature and humidity sounders to the observing system and moreover, continued positive impact is still found from the adding the latest sounders to the robust full observing system (Duncan and Bormann, 2020). However, with some satellites having already been in flight for many years combined with a lower frequency of new missions supporting high performance MW sounders, the constellation as it stands now is expected to decline in the coming years.

Recent advances in technology have allowed the possibility of launching MW sounding instruments on small satellites without undesirable levels of reduction in performance compared to the currently used satellites. While some compromises remain with the compact instruments, such as potential loss of lower frequency wavelengths (below 50GHz), a significant advantage of the small satellites is that they provide a cost-effective solution to provide higher temporal sampling MW observations. Such constellations are anticipated to become an important presence in the future observing system (World Meteorological Organisation, 2019) while complementing the continued use of instruments on the larger satellite platforms.

As momentum gathers behind the development and launch of small satellites, it is important at an early stage in the constellation design to consider the balance between the benefit to Numerical Weather Pre-

diction (NWP) against practicalities such as instrument limitations and cost. In this study, various options for a possible new constellation of small satellites carrying MW sounding instruments are evaluated to explore two aspects of design optimisation:

- What is the optimal number of satellites and their orbit type (e.g. polar or lower inclination orbits)?
- What are the relative benefits of humidity sounding channels (around 183-GHz) only vs. a combination of humidity and temperature sounding (50-60-GHz) channels?

In the first question posed here, additional observations from a small satellite constellation are attractive given the continued benefit seen from adding existing MW sounders (Duncan et al., 2021). The cost-effective nature of the small satellites means there is potential to have many more MW sounders in orbit than are currently available. The change in impact from continuing to add data is expected to slow as it becomes increasingly challenging to extract more benefit with more observations, to the point that adding further data may not be cost-effective. In this study, a range of constellation sizes is tested which goes significantly beyond the number of satellites already assimilated, allowing investigation of the shape of this trend to provide an indication of the NWP benefit against cost. Different orbit types (sun synchronous or inclined orbits) can be used to examine the influence of different observation sampling distributions while a combination of orbit types could probe whether this is cost effective than more satellites in the same orbit type.

Regarding different sets of channels on the instrument, the benefit from higher temporal sampling will be realised in different mechanisms for the humidity or temperature sounding. Low instrument noise for temperature sounding channels is crucial as the data must correct NWP temperature fields that are already very accurate (within the order of tenths of Kelvin) particularly in the troposphere (Bell et al., 2008). However, by repetitive measurement the small satellites could reduce the effective noise to achieve a greater positive impact. Meanwhile the higher temporal sampling with humidity sounding channels could contribute to better observing faster evolving cloud and humidity features. Furthermore, the higher frequency humidity sounding channels are more easily accommodated on small platforms and their benefit in assimilation is not so limited by noise performance. Testing potential constellations with a choice of either humidity only or temperature and humidity channels will seek to better quantify the value of including temperature sounding capability on future MW sounders. Note that when referring to testing "humidity only" in this study, for effective use of the 183-GHz sounding channels, the presence of window channels around 89-GHz and 165-GHz is also required. While they are not currently directly assimilated, they are crucial for providing information related to emissivity and cloud amount. For the temperature sounding channels, window channels at lower frequencies in the 50-GHz band (e.g. at 50.3-GHz and 52.8-GHz) are able to fulfil this role.

The benefit to NWP of different configurations of small satellites carrying MW sounding instruments can be assessed using an Ensemble of Data Assimilations (EDA) method. EDA experiments concerning simulated satellite data have in the past been used at ECMWF to successfully evaluate the impact of increasing numbers of Global Navigation Satellite System (GNSS) Radio Occultation (RO) observations (Harnisch et al., 2013; Lonitz et al., 2021) and the benefit from Aeolus (Tan et al., 2007). The EDA method is applied here to determine the relative benefit of each of the possible constellations where MW data have been simulated for each scenario. Further EDA experiments that change the number of existing MW observations only also lend context to the results where simulated data have been added.

This final report summarises the overall outcomes of the ESA project investigating the optimal design of a potential future constellation carrying MW sounders. It provides an overview of and builds on the activities described in detail in earlier work package reports (Lean et al., 2021a,b, 2022) and includes new

results from the EDA spread analysis conducted in the subsequent work package. A brief overview of the EDA method is described in section 2 where the details of the technical set up of the EDA experiments are also given. How to relate the EDA impact to traditional measures of forecast error is also considered. The potential constellations subsequently tested are listed and discussed in section 3. The MW data are simulated and assimilated following the technical set up described in section 4 where much of the existing, well-established infrastructure of using existing MW data has been utilised. Results from the EDA experiments are presented in section 5 and finally, in section 6 a summary and implications for optimising the future design of a constellation are considered.

2 Use of the Ensemble of Data Assimilations to assess observation impact

In the following, we summarise the use of the EDA for the estimation of the impact of future observations, encompassing and building on the work presented in WP-1000 (consolidation) and WP-2000 (calibration). For further details see Lean et al. (2021a,b).

2.1 Methodology of the EDA

The EDA is used at ECMWF and elsewhere to represent random uncertainties in analyses and short-range forecasts of large NWP systems (Isaksen et al., 2010). It uses a Monte-Carlo approach to estimate the statistical characteristics of errors in analyses and short-range forecasts from the uncertainties in input parameters and the forecast model. This is done by running a finite number of independent cycling assimilation systems, in which observations and the forecast model are perturbed to generate different inputs for each member. The following aspects are perturbed in the EDA:

- Observations: These are perturbed according to the observation error covariances assigned in the assimilation system, assuming a Gaussian distribution with zero mean (Isaksen et al., 2010).
- Forecast model: Model error is represented by stochastic perturbations of the model physics (carried out using the Stochastically Perturbed Parametrised Tendency (SPPT) scheme, (Palmer et al., 2009)).
- Sea surface temperature (SSTs): These are perturbed according to climatological error structures.

Mathematically, the errors from the perturbed realisation of 4D-Var evolve with the same equations as the errors of the unperturbed version (see Lean et al. (2021a) which provides a summary of the mathematical details). A crucial measure of the EDA is the ensemble spread, i.e. the standard deviation of the ensemble members around the ensemble mean. If the characteristics of the perturbations in the ensemble members correctly represent the true errors, the spread of the ensemble will reflect the errors in analyses and forecasts. At ECMWF, the EDA method has been operationally used since June 2010 (Isaksen et al., 2010; Bonavita et al., 2011) to fulfil two key requirements:

- Specification of background error statistics: The EDA is used to provide climatological as well as flow-dependent estimates of the statistical properties of the errors in the short-range forecasts (background) used in the high-resolution deterministic assimilation system. To capture flow-dependent aspects, an EDA is run alongside the high-resolution deterministic forecast system.

- Initialisation of the ensemble prediction system: Perturbations from the EDA are used together with Singular-Vector methods to initialise ECMWF's ensemble prediction system which provides probabilistic medium-range forecasts.

Operationally, 50 EDA members are currently used at ECMWF. The number of members used in the ensemble is a trade-off between computational affordability and reducing sampling noise in the background error estimates. For research-purposes EDAs with 10 members have been found to provide adequate estimates, at least for background error variances on larger scales.

2.2 Application of the EDA to simulate impact of future observations

The EDA method also provides a means of assessing the impact of potential future observations on analysis and short-range forecast error statistics. This is done by investigating how the spread of the ensemble changes as we add new observations. The future new observations need to be simulated, for instance from high-resolution NWP analyses, whereas real observations can be used for all other observing systems. Expected error characteristics for the new observations are represented through applying appropriate perturbations in the EDA. When assessing changes in the observing system, a positive impact arises when the ensemble spread is reduced, indicating improved analysis/forecast error statistics.

The approach has been first developed by Tan et al. (2007) to simulate the expected impact of wind profile observations from Aeolus, and it has been subsequently applied by Harnisch et al. (2013) to study the expected benefits from further GNSS-RO observations. The latter study characterised the expected impact from a hypothetical constellation of GNSS-RO observations, and estimated the expected benefit as the number of observations increased, therefore providing input for determining a cost-effective target for the evolution of the GNSS-RO constellation. In recent work, Lonitz et al. (2021) used increases in real GNSS-RO observations to further evaluate the method, showing that the relative increase in the impact of GNSS-RO data predicted in Harnisch et al. (2013) was in fact in line with the benefits obtained with real data.

The EDA method has similar aims as the more traditional Observing System Simulation Experiments (OSSEs) (Arnold and Dey, 1986; Masutani et al., 2010). In these, simulated observations are generated from a "truth" - the "nature run" - and subsequently assimilated in an alternative forecast system (e.g. Masutani et al. (2007)). To achieve this, all the observations from both the existing and proposed new sources need be simulated, including their full error characteristics. This means that OSSEs can be problematic if errors are not adequately modelled for all observations. OSSEs are also computationally expensive, as long periods are required to establish statistically robust results. Meanwhile Tan et al. (2007) and Harnisch et al. (2013) both used relatively short EDA experimentation periods, of the order of one month, which was motivated by relatively stable characteristics of the EDA spread. OSSEs and the EDA method are seen as complementary (Harnisch et al., 2013).

The EDA method can also be thought of as a 4D-Var theoretical error covariance/-information content study. Computing 4D covariance matrices directly is not practical due to the very large matrix dimensions required. However, the spread in the ensemble members provides an estimate of analysis/forecast error statistics of the 4D atmospheric state which includes the impact of a complex observing system and forecast model. Therefore, one of the key differences in the metrics available from OSSEs and the EDA method is that the former evaluates one specific realisation of forecast error, evaluated against the "truth" from the nature run, while the latter aims to evaluate directly the statistical characteristics of the forecast error.

The EDA method is of course also not free from limitations either. Firstly, the method assumes that the perturbations applied in the EDA reflect the true error characteristics, but in practice these are both subject to their own uncertainties. Secondly, the EDA is a Monte Carlo method so the true values are only found in the limit of an infinite ensemble. This results in sampling errors from a finite ensemble size (Bonavita et al., 2011) and systematic errors can arise from incorrectly estimated error covariances (e.g. Cardinali et al. (2014)). By averaging over larger areas, such as hemispheric scales, small scale sampling errors can be reduced while keeping the large-scale changes in the EDA spread. Harnisch et al. (2013) also note that we can assume the systematic errors are similar across a set of experiments run with consistent settings and therefore the magnitudes of relative changes are unaffected. Finally, for both the EDA and OSSE methods, both can only assess the impact reflecting the current treatment of the observations. Neither system can account for the impact of unknown future developments that could potentially change the priorities in MW sounder design, or similarly for investigating impacts of other observation types.

2.3 EDA experimental set up

The EDA experiment configuration used throughout employs a $T_{Co}399$ (25km) resolution grid with 137 vertical levels and three inner loops at a resolution of $T_L95/T_L159/T_L255$, and it comprises the control run and 10 perturbed ensemble members. This is a standard configuration of the EDA used at ECMWF for development testing and experimentation for future observing systems. A total of four weeks will be used for running each EDA experiment to test different scenarios of future instruments. This four-week period includes a one-week spin-up period needed for the EDA to develop representative levels of spread which will be discarded. As established in WP-1000 and reported in Lean et al. (2021a), the remaining three weeks was found to be adequate to obtain reliable estimates of EDA spread changes. The choice is consistent with findings in Harnisch et al. (2013). The period of 1 - 28 June 2018 was chosen which makes use of a period with a good and stable coverage from heritage MW sounding instruments. Throughout this study, unless otherwise stated, we use the short-range EDA spread values initially computed at a resolution of T_L255 (the highest resolution inner loop of the experiment) and at T+12 hours, as short lead times are expected to exhibit the most robust signals. As the forecast length increases, model uncertainties increase, reducing the clarity of signals introduced by observation changes (Harnisch et al., 2013).

2.4 Relating EDA spread change to forecast error

In the following, we evaluate the link between changes in EDA spread and more traditional measures of forecast impact given by Observing System Experiments (OSEs). In OSEs, the measure of observation impact is the reduction of the forecast error between assimilation experiments with and without selected observations. The comparison of results from OSEs and EDAs is sometimes referred to as a calibration step. However, the aim here is not to infer an exact, quantitative relationship. Rather, this step provides evidence of the strong links between a reduction in the EDA spread and a reduction in the standard deviation of forecast error seen in OSEs. It confirms the change in EDA spread as an appropriate means to measure observation impact and gives confidence in reference points using real data against which the addition of the small satellite data can be compared. It can be useful in particular to assess systematic effects on the EDA spread, for example, resulting from an under-dispersive ensemble. In this case, the ensemble spread is smaller than the corresponding forecast error which is a known characteristic (Bonavita et al., 2012) for example, relating to imperfect generation of the perturbations for each ensemble member. Results from Harnisch et al. (2013) supported the under-dispersive nature of the EDA

although the forecast error reductions from the OSEs were found to generally be in good agreement with the reductions in the EDA spread.

In calculating the forecast error for an OSE, the reference is typically an analysis produced by an NWP system, or a set of observations, such as radiosondes. A reduction in the standard deviation of the differences between forecasts and the reference between experiment and control indicates an improvement. To compute the forecast error in OSEs, the estimation of short-range forecast errors using analyses can be problematic, as the size of the errors in the analyses and forecasts is comparable and taking full account of the errors in the analysis is largely impossible. When using the radiosondes as a reference, differences from the forecast are often referred to as O-B where B, the model background, is the 12-hour forecast from the previous model cycle. Such comparisons are also not free from difficulties. Firstly, radiosondes do not sample the globe homogeneously, and in particular do not capture well forecast quality over oceans or other remote areas. Secondly, the effect of observation errors has to be taken into account when comparing observation-based forecast error estimates, as it is a sizeable component of the differences between forecasts and observations.

Two techniques have been applied to investigate the links between EDA spread and OSE forecast error using the impact of changes in existing MW observations using:

1. Pre-existing separate 3.5 month (1 Jun - 15 Sept 2018) OSEs which were performed alongside EDA experiments (Duncan et al., 2021) which both compare an observing system with seven pairs of MW temperature and humidity sounding channel sets with a no MW sounder baseline.

2. Four shorter, one-month EDA experiments run as part of this study (see table 1 later) where OSE-like statistics can be produced by verifying only the control member of the different cycling assimilation systems for the respective experiments.

Both techniques use radiosondes as a reference to calculate the OSE forecast error and explore in different ways a proposed linear relationship between the EDA variance (the square of the EDA spread) and the OSE forecast error given by the variance of the radiosonde O-B. In the following, we will start by discussing the long experiments outlined in the first point which are used to analyse the vertical structure more closely and compare the change in EDA spread to the OSE impact. Further details of this evaluation can be found in Lean et al. (2021b). In the second part, the availability of four different experiments allows us to further probe the mathematical relationship between the EDA variance and variance of the radiosonde O-B similar to work conducted using GNSS-RO data in Lonitz et al. (2021). Here, we consider the correlation between the two quantities which should be linearly related.

In using the pre-existing EDA experiments, spread values are available at a forecast lead time of T+3, averaged on a 1° x 1° grid and area weights applied to calculate the EDA changes for different geographical regions. The standard deviation of radiosonde departures from an OSE is used as a measure of forecast error, and changes to these standard deviations can be linked to changes in the EDA spread. To do this, we recall that the standard deviation of radiosonde O-B reflects the true radiosonde observation error σ_o and the true background error σ_B as follows, provided the two errors are uncorrelated:

$$Std.dev.(O-B) = \sqrt{\sigma_B^2 + \sigma_o^2} \tag{1}$$

If the EDA adequately represents errors in the background, we hence need to include an estimate of the observation error for radiosondes to be able to compare the two quantities. Estimates of the observation errors for the radiosondes have been provided by B. Ingleby (pers. comm., 2021). They have been generated over the period Nov 2016 - Feb 2017 using the Desroziers diagnostic technique (Desroziers

et al., 2005) based on the Vaisala RS92 and RS41 radiosondes which are known to be a good quality instrument type (Dirksen et al., 2014; Ingleby, 2017). As T+3 spread values are used here, it is possible that there is an underestimation of the background error compared to the T+12 values. However, with both being at very short lead times, the difference is expected to be small.

The reductions in EDA spread resulting from adding observations are found to be broadly consistent with forecast error reductions in corresponding OSEs when evaluated against radiosondes, provided radiosonde observation errors are taken into account. Here, the calculation is repeated for the control and experiment in order to compare the expected normalised difference for the radiosonde fit using EDA values with the actual OSE values. Figure 1 shows that the agreement appears particularly good for the lower and mid troposphere, whereas the statistics suggest that the EDA may underestimate the impact in terms of temperature and wind in the stratosphere. Not all of the vertical structure is captured by the estimated values and there are some differences in the magnitude. Using this technique, within the uncertainties of forecast-error estimation, the reductions in the EDA spread resulting from adding existing observations compare favourably with reductions in forecast errors seen in OSEs. At the same time, it is also clear that there is not a one-to-one correspondence, and at times the EDA spread reductions can be prone to under-estimating the impact seen.

The above comparisons rely on a separately provided estimate of the radiosonde observation error. To avoid this, we can also investigate more generally the link between EDA spread reductions for a series of EDA experiments with real data, and relate these to forecast error reductions seen in an OSE. To do this, we use the four EDA experiments with changes in the use of real MW observations (table 1). We again use radiosonde departures from short-range forecasts as a measure of forecast accuracy. Lonitz et al. (2021) has performed similar evaluation for GNSS-RO observations.

In general, there is a trend for increasing variance of the radiosonde O-B with variance of the EDA spread such as in the examples shown in figure 2. The broadly linear relationship suggests that relative changes in the EDA spread compare well with results from OSEs. Although the sample is small, the strength of this correlation varies with geographical regions and levels. For example, the relationship tends to be stronger at levels where the MW data exert most influence (mid/upper troposphere/lower stratosphere) and where radiosonde coverage is also denser in the northern hemisphere. In contrast, the relationship is weaker for the low troposphere in the tropics (not shown).

To evaluate the relationship more quantitatively, we can perform a regression for the points shown, introducing a scaling factor m for the EDA spread, addressing the known under-dispersiveness of the EDA:

$$\sigma^2_{o-b} = m * s^2_{EDA} + c \tag{2}$$

Comparison to equation 1 reveals that c is in this case an estimate of the radiosonde observation error variance.

For most areas and geophysical parameters, the regressions show slopes of greater than one, that is, the forecast impact as measured by the radiosonde departures is larger than suggested by the EDA spread reduction. This reflects the known under-dispersive nature of the EDA. This is consistent with the findings in Lonitz et al. (2021), though the use of different seasons and different experimentation periods mean that the scaling factors cannot be directly compared.

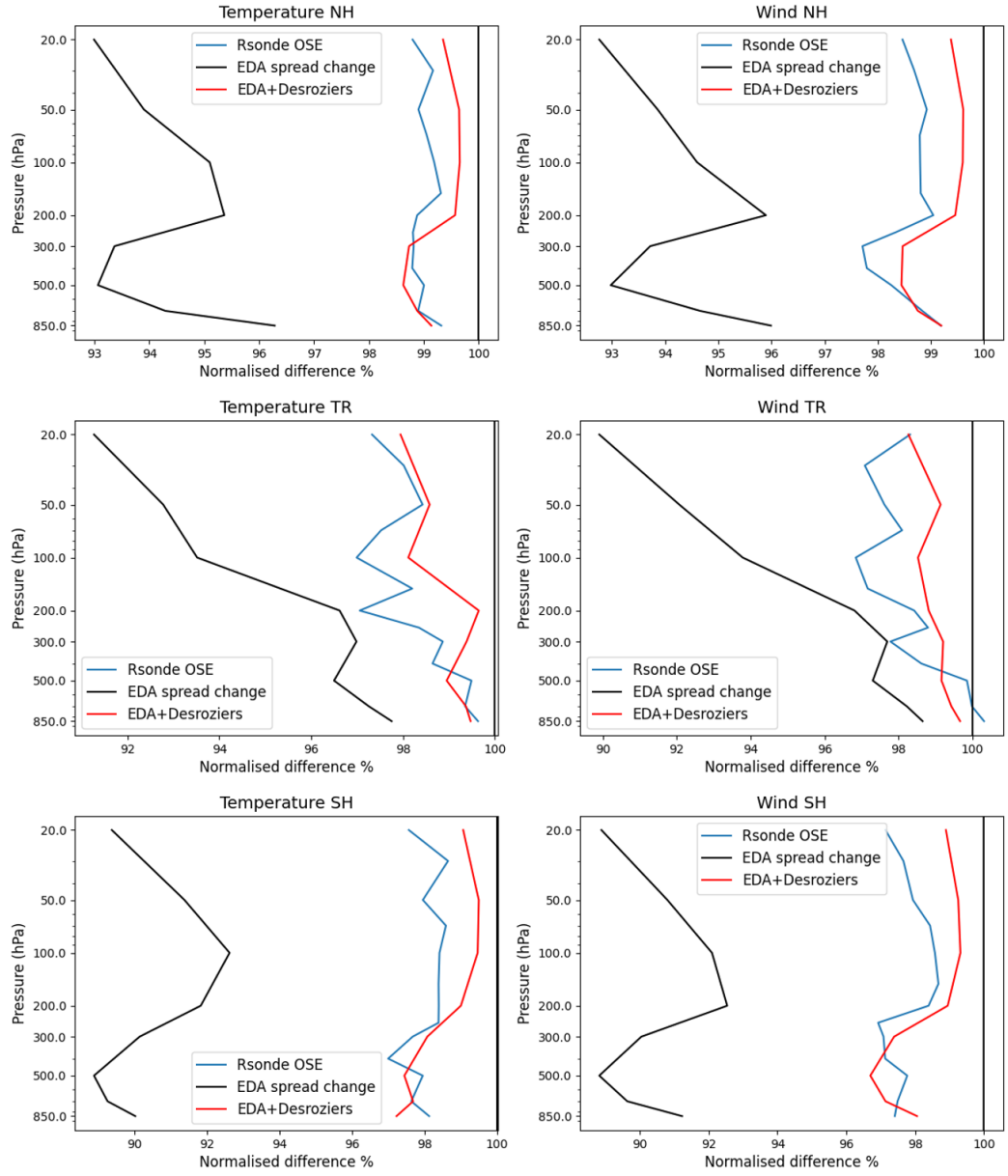

Figure 1: Normalised difference in standard deviation of O-B departures for temperature (right) and u wind component (left) using values directly taken from the OSE verification (blue line) and the estimates of the same statistics generated with equation 1 (using the EDA spread (representing σ_B) and Desroziers observation errors (representing σ_O)) calculated separately for the control and experiment (red line). Here the control uses the full observing system but with no MW sounders and is compared to an experiment where seven pairs of MW temperature and humidity sounding channel sets are added. The normalised change in the EDA spread reduction (black line), which does not account for observation error, is shown for reference. Data are shown averaged over the northern hemisphere and from 8 Jun - 15 Sept 2018.

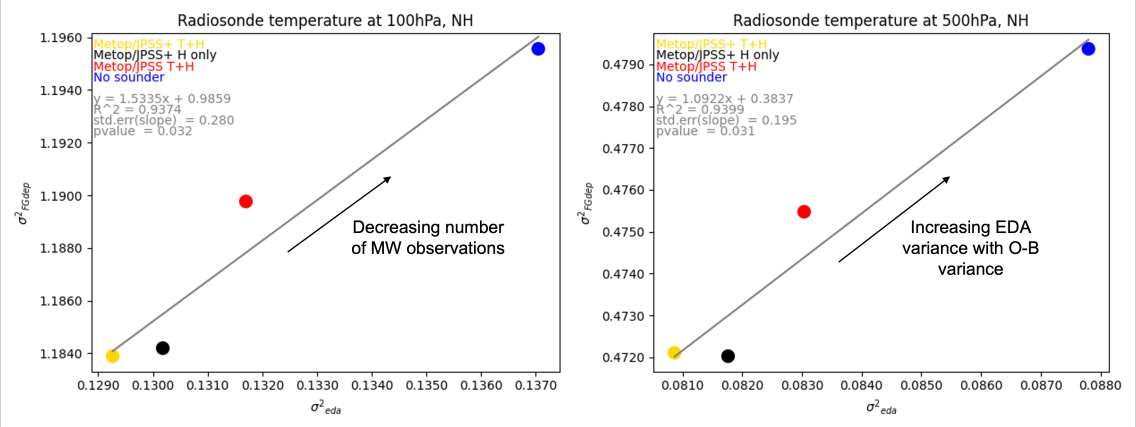

Figure 2: Scatter plots of the variance of the radiosonde (O-B) versus the variance of the EDA spread for temperature, 100 hPa (left) and U wind, 200 hPa, (right) both for the northern hemisphere. Different colour dots are used to differentiate the experiments as detailed later in table 1. Estimated values for the scaling factor and constant in equation 2 are also given in the equation on each plot.

3 Potential future constellations

In this study, key factors being considered towards the optimal design of the constellation of small satellites are the number and distribution of the satellites and the relative importance of humidity and temperature sounding channels. A range of potential constellations is required to probe these design choices. To use the EDA method, each scenario is tested by adding the simulated small satellite data to a baseline observing system of existing observations. Here the baseline consists of the full observing system but with MW sounding only from the Metop and the JPSS systems, that is two pairs of Advanced Microwave Sounding Unit - A/Microwave Humidity Sounder (AMSU-A/MHS) on Metop-A/B and two Advanced Technology Microwave Sounder (ATMS) instruments on SNPP and NOAA-20. This Metop/JPSS baseline reflects a possible future conservative observing system where the number of larger, high performance MW platforms has been reduced. These 01:30 and 09:30 orbits are a high priority to maintain (Coordination Group for Meteorological Satellites, 2022). The observing system otherwise benefits from the assimilation of window channels from three MW imagers in the all sky framework, five hyperspectral infrared instruments including from platforms in the Metop and JPSS orbits and other significant observing system components including radio occultation, atmospheric motion vectors and conventional observations such as radiosondes and aircraft.

To provide points of reference for the impact of the simulated data, four EDA experiments were run where changes were made only to the existing set of MW sounding instruments. Table 1 lists the configurations used which range from denying all MW sounding data to a maximum of having seven pairs of temperature sounding (50-60-GHz) and humidity sounding (183GHz) channel sets.

For the potential future small satellites, we consider here a set of six constellations (Table 2). These were devised in an ESA partner project and further details on the sampling characteristics and constellation considerations can be found in JCR Systems (2022). Constellations include three with purely polar orbiting platforms, two with purely lower inclination (60°) orbits and one which contains a mixture of orbit types allowing some insight into the effect of changing the distribution. The number of small satellites ranges from 8 to 20 to investigate how the magnitude of the impact changes when moving to much larger constellations than we currently have available. Each scenario is also tested with humidity

Table 1: Combinations of existing MW sounders (all on sun synchronous platforms) used in baseline experiments containing only real data evaluated using the EDA method. For B3 and B4, a set of 183GHz humidity sounding channels is provided by the Special Sensor Microwave Imager/Sounder (SSMIS) instrument on the F-17 platform. Appropriate window channels are also employed to effectively assimilate the humidity channel sets. LECT = Local Equator Crossing Time.

Baseline no.	Experiment name	MW sounder platform	LECT
B1	No sounder	None	-
B2	Metop/JPSS	Metop-A/B, SNPP, NOAA-20	2 x 09:30, 2 x 01:30
B3	Metop/JPSS+ (temp + hum)	B2 + NOAA-15/-18/-19, F-17	2 x 09:30, 2 x 01:30, 2 x 06:30, 1 x 04:00, 1 x 08:00
B4	Metop/JPSS+ (hum only)	B2 + NOAA-18/-19, F-17	2 x 09:30, 2 x 01:30, 1 x 06:30, 1 x 04:00, 1 x 08:00

Table 2: Potential future constellations of small satellites carrying MW sounders evaluated using the EDA method. Each of the small satellite constellations are added to the Metop/JPSS baseline (B2, table 1) and are run with humidity sounding channels only (plus complementary window channels) and separately with both temperature and humidity sounding channels used. LECT = Local Equator Crossing Time.

Scenario no.	Experiment name	Orbit type	No. of planes	No. of satellites
1	Polar	SSO: LECT at 03:30, 05:30, 07:30, 11:30	4	8
2	Polar+	SSO: LECT at 02:50, 04:10, 05:30, 06:50, 08:10, 10:50, 12:10	7	14
3	Polar++	SSO: LECT at 02:30, 03:30, 04:30, 05:30, 06:30, 07:30, 08:30, 10:30, 11:30, 12:30	10	20
4	4x2	Inclined 60°	4	8
5	6x2	Inclined 60°	6	12
6	Polar & 4x2	Mix SSO and 60°	8	16

sounding channels only (with complementary window channels) and separately with both humidity and temperature to study the relative benefits. The baseline experiments with real data also provide valuable intermediate data points between the Metop/JPSS baseline and the smallest small satellite constellation which has a total of 12 platforms with MW sounders.

An optimisation is performed (JCR Systems, 2022) to determine the Local Equator Crossing Time (LECT) of the orbital planes of the small satellites and their separation and phasing, while accounting for the Metop and JPSS orbits. A key aspect of choosing these parameters was the speed at which the global spatial coverage accumulated and revisit times. This led to using two satellites per orbital plane at 180° separation and, for the polar orbiting satellites, having the location of the two satellites around

each orbit in phase across the different orbital planes such that e.g. all of the satellites sample the polar regions around the same time.

The instrument specifications for the potential MW sounder on a small satellite tested here use the Arctic Weather Satellite (AWS) instrument as a basis. AWS is a small satellite proposed for a future constellation (e.g. https://www.esa.int/Applications/Observing_the_Earth/Meteorological_missions/Arctic_Weather_Satellite, Lagaune et al. (2021)) and provides a compromise between the extent of miniaturising the instrument (the mass is expected to be around 120kg) and retaining good performance and characteristics similar to the existing MW instruments. Table 3 summarises key instrument characteristics for the small satellite design used in this study. The small satellites across all the proposed scenarios use a sub-selection of channels available on the future MicroWave Sounder (MWS) which are also largely in common with AWS and AMSU-A/MHS. Similar to AWS, the envisaged small satellite MW instrument is a cross track scanning radiometer with a maximum scan angle set at 54.4°. The altitude of the spacecraft is allowed to vary slightly between constellations for optimal coverage but remains close to 600km. The number of scan positions also varies slightly with 113, 114 and 104 used for the Polar, 6x2 and remaining constellations respectively. Differences were introduced when optimising the temporal-geospatial coverage at different altitudes. Noise performance estimates for each channel are generated using estimates of the instrument performance including scan rotation rates and receiver technology such as spectral resolution and thermal stability. Further details on the constellation and instrument design and Noise Equivalent Differential Temperature (NEDT) derivation can be found in (JCR Systems, 2022). Note that the noise values used for this study are often referred to as the sample (or raw) NEDT which accounts for the integration time for one FOV on the instrument. These estimates are typically larger than values where the time for the antenna to cover an angle equal to the 3dB beam width is used in the calculation (e.g., Atkinson (2015)).

Some small satellites carry a suite of channels at 118GHz or higher frequency channels beyond 183GHz. For this study, we choose to focus on frequencies around 50 and 183GHz which have very mature use at ECMWF. Developing capabilities to assimilate new e.g. higher frequency channels to extract optimal and realistic benefit is not a trivial exercise. Use of well-established frequencies allows exploitation of much of the existing infrastructure to simulate/assimilate the small satellite data. As this study is the first application of the EDA for a future MW instrument, we can already have confidence in the realistic processing of the proposed new instrument and perform a more direct comparison at this stage to impact from existing MW observations. Future work can be envisaged which would look to build on this foundation for newer capabilities.

4 Framework for simulating and assimilating small satellite data

The framework for the simulation and assimilation of the small-satellite data has been established in WP-3000 (system development) and details on the system design and the relevant choices can be found in Lean et al. (2022). In the following, we recap the main steps.

The brightness temperatures (BTs) for the small satellite data are simulated from high-resolution ECMWF fields, using a tailored configuration of the Integrated Forecast System (IFS). To achieve this, the IFS has been modified to process data from the new sensor on-board the small satellites. The spectral channel characteristics are modelled on MWS, and the processing replicates as far as possible that of the all-sky assimilation of existing MW sounding data (Geer et al., 2014; Duncan et al., 2022). As in the operational ECMWF 4D-Var assimilation system, the processing is done in 12-hour windows. Within these 12-hour windows, we use the forecast model combined with a radiative transfer model to provide physically con-

Table 3: Specifications for channels used in the small satellite simulation. Note that the values of instrument noise correspond to the sample NEDT which are scaled values of the 3dB Field of View (FOV) NEDT, accounting for the sampling interval of the instrument rather than using the time for the antenna to cover an angle equal to the 3dB beam width.

Centre frequency (GHz)	MWS channel	AMSU-A/MHS channel	Bandwidth (MHz)	Footprint size at nadir (km)	Sample NEDT (K)
50.3	3	AMSU-A 3	180	40	0.85
52.8	4	AMSU-A 4	400	40	0.60
53.596±0.115	6	AMSU-A 5	2x170	40	0.60
54.4	8	AMSU-A 6	400	40	0.60
54.94	9	AMSU-A 7	400	40	0.60
55.5	10	AMSU-A 8	330	40	0.65
57.290344	11	AMSU-A 9	330	40	0.65
89	17	AMSU-A 15/MHS 1	4000	20	0.25
164-167	18	MHS 2 (157GHz)	2800	20	0.55
183.311±7.0	19	MHS 5	2x2000	10	0.65
183.311±4.5	20	-	2x2000	10	0.65
183.311±3.0	21	MHS 4	2x1000	10	0.80
183.311±1.8	22	-	2x1000	10	0.80
183.311±1.0	23	MHS 3	2x500	10	1.05

sistent values of model equivalents at the observation locations in space and time. The process replicates that used during the assimilation of real MW observations. For this study, observations are simulated from an analysis trajectory (i.e. the result of assimilating all other observations during the 12-hour window). The simulated BTs are generated using a version of the IFS based on cycle 47R3.0 which has been adapted to include the latest package of MW improvements that will be used operationally at the next IFS cycle upgrade. The key steps in the flow of data leading to the assimilation of the small satellite are outlined next to include the simulation process, thinning steps, addition of noise and the observation error model construction.

4.1 Simulating MW brightness temperatures

High resolution ($T_{Co}1279$, ∼9km, 137 vertical levels) ECMWF analyses (using cycle 47r1.4 of the Integrated Forecast System (IFS)) are used as a proxy for the truth. The translation between model quantities and BT is carried out using a radiative transfer model. RTTOV-SCATT[1] (version 13) is used here which accounts for scattering from hydrometeors at MW frequencies and therefore allows use of the MW data in the all sky framework (Saunders et al., 2020; Geer et al., 2021). For producing the simulated observations here and later during assimilation, we use coefficients generated for MWS as a subset of the same frequencies/polarisations are proposed for the small satellites (as detailed earlier in table 3). The input to RTTOV-SCATT consists of a model profile interpolated to the geo-location provided in a constellation

[1]RTTOV = Radiative Transfer for TOVS, TOVS = TIROS Operational Vertical Sounder, TIROS = Television Infrared Observation Satellite

sampling file (these spatial/temporal sampling files were externally provided through work detailed in JCR Systems (2022)), taking the slanted viewing geometry into account (Bormann, 2017). The spatial extent of the satellite footprint is not explicitly modelled.

The process is very similar for simulating the small satellite data or generating model equivalent BTs for real MW data. However, over land, snow and sea-ice surfaces, a different strategy is required as for real MW sounding data an emissivity is derived using the observations from window channels. The alternative approach applied to the small satellite simulation uses an emissivity atlas over land and relatively crude estimation over the more difficult snow and sea ice surfaces which will not capture the full variability and complexity of the emissivity variations over these regions. Further details are discussed in Lean et al. (2022). In the later assimilation step, the dynamic retrieval can be employed again as the simulated BTs will be present in the required window channels. The retrieved emissivities for the small satellite data are not consistent with those from other MW sounders, but since there is no interaction between different emissivity retrievals in the IFS this is not considered a major problem. However, no attempt is made at modelling biases related to biases in the effective model skin temperature which can be considerable over snow and sea-ice. As a result of these approximations, the simulation of the impact of the small satellite data over snow and sea-ice surfaces is hence likely to be optimistic.

At this stage in the processing, no error sources have been included in the BT simulation. These are added, based on sample NEDT values, in a later step (see section 4.3). Figure 3 shows the simulated BTs using the small satellite configuration alongside the bias corrected real BTs from the equivalent channel on the Metop-B AMSU-A/MHS instruments. The similar atmospheric structures and overall good agreement support the method of simulation.

4.2 Sampling and thinning

The scanning pattern for the potential small satellite instrument is designed to oversample meaning considerable overlap between adjacent fields of view (FOVs). ATMS has a similar oversampling scan pattern and employs a '3x3 averaging' scheme where nine FOVs are averaged using 3 neighbouring scan positions and scanlines (Bormann et al., 2013) prior to assimilation. This strategy is particularly useful for temperature sounding channels to effectively reduce the sample noise and make it a more comparable magnitude with the errors to be corrected in NWP. A similar 3x3 averaging technique is applied here to the small satellite data. Further details regarding the choice of the number of FOVs to average and the resulting spatial sampling and footprint sizes can be found in Appendix A.

In addition to the 3x3 averaging, prior to assimilation, the small satellite data are thinned in space and time. All MW sounding data at ECMWF undergo this thinning to mitigate against the presence of spatially correlated observation errors, primarily arising from representation errors (e.g. radiative transfer errors, errors due to differences in the spatial scales that are represented). It is currently technically not possible to account for such spatial observation error correlations during the assimilation, and the applied thinning mitigates against overfitting the assimilated data.

Thinning for the small satellites is designed to replicate the choices made in the all-sky assimilation of real MW sounding data. The thinning is based on selecting, within a specified time-slot, the observation closest to a reduced Gaussian grid point (T_L255 grid) then selecting alternate grid points in the meridional direction. This results in a minimum separation distance of around 110km. For the small satellite data, the same thinning scale is employed for humidity and temperature sounding channels. In line with the assimilation of AMSU-A, the time-slot is set to 30 min, and observations from all satellites of the small satellite constellation are thinned together. That is, only data from the closest location across all the small

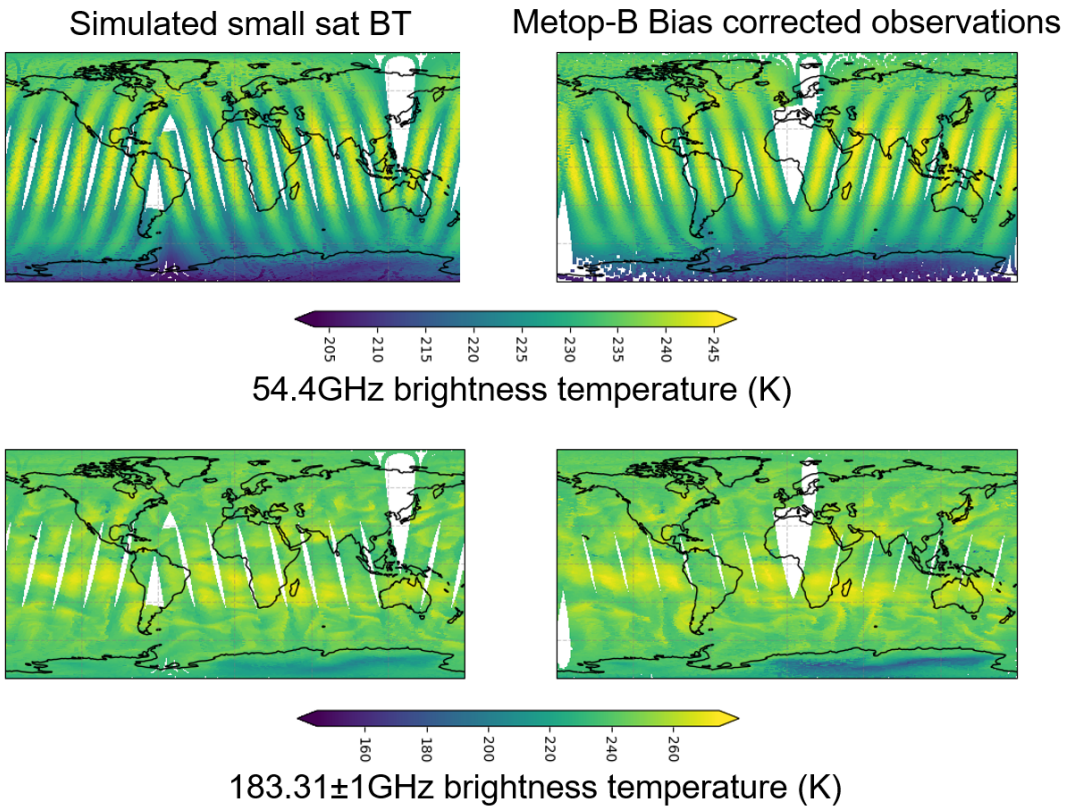

Figure 3: Simulated brightness temperatures (left) for a constellation containing eight small satellites across four orbital planes in sun synchronous orbits compared to equivalent bias corrected observations (right) from Metop-B AMSU-A and MHS. The tropospheric temperature sounding channel at 54.4GHz (top) and humidity sounding channel at 183.31±1GHz (bottom) illustrate the realistic values and structures seen across all the channels in the simulated data. Data are for one 12-hour cycle on 2 June 2018.

satellites is selected per Gaussian grid point, within a half-hour interval. This means that where there is more spatial overlap from different satellites within the time interval, a higher proportion of data are lost through the thinning process.

For the polar orbiting satellites, the interaction between the satellite phasing and thinning results in a higher proportion of data thinned out in the polar regions due to considerable overlap in the orbits. Higher data density over the high latitudes for these scenarios containing only sun synchronous orbits is expected. Figure 4 shows the locations of MW sounding locations after the thinning process is complete for the six constellations tested. While for the Polar/Polar+ scenarios it is clear that the highest densities lie above around 70°N/S, the Polar++ shows relatively uniform coverage across the globe as a result of this phasing/thinning interaction. For the inclined orbits, observations are densest around 60-75°N/S as the phasing is such that there is actually little overlap between the satellites within the 30 minute thinning windows. Meanwhile, in the tropical latitudes, the polar orbits provide a slightly higher observation density than an equivalent number of satellites in inclined orbits.

4.3 Adding noise to simulated observations

Prior to assimilating in the EDA, perturbations are added to the simulated observations to simulate instrument noise and potentially other error sources. For each observation, a random number is drawn from a Gaussian distribution with mean of zero and standard deviation of one. This is multiplied by the estimate of sample NEDT divided by three (due to the averaging described in section 4.2) of the associated channel on the instrument to generate the final perturbation. Therefore, channels with higher noise estimates such as the humidity sounding channels generally have perturbations larger in magnitude than those of the lower noise temperature sounding channels.

It should be noted here that these noise-affected simulated observations are further perturbed in the EDA, with different perturbations in each EDA member to sample the uncertainty in the observations. These perturbations in the EDA will be consistent with the observation error model used in the assimilation. A sensitivity test was run using the Polar constellation of small satellites in which two EDA experiments were run with either perturbed or unperturbed simulated BTs and compared to the Metop/JPSS baseline. In this case, the formulation of the observation error model and therefore the basis for the perturbations generated within the EDA was not changed. The effect of the initial perturbations applied had very little impact on the overall changes in EDA spread compared to the overall signal (not shown). This suggests that the perturbations added in the EDA, which larger than the NEDT values, are the main factor affecting the spread of the EDA.

4.4 Observation error model adaptation

Accurate estimates of observation errors for the small satellites are important for both determining the weighting during assimilation and the perturbations applied during the EDA. Simulated data from humidity and temperature sounding channels on the small satellites are used in the all-sky framework at ECMWF (Geer et al., 2010, 2017). The all-sky observation error model has been successfully used for many years and continues to be applied to the latest all-sky MW data. The observation error typically comprises of measurement error, such as originating from instrument noise, the forward model error, e.g. from the radiative transfer calculations, and representation error, arising from different scales and processes being represented in the observations and the model fields. In the case of all-sky use, the representation error dominates the observation error in cloudy conditions, arising from different representativeness of clouds in the observations and the model fields. This is accounted for by an observation

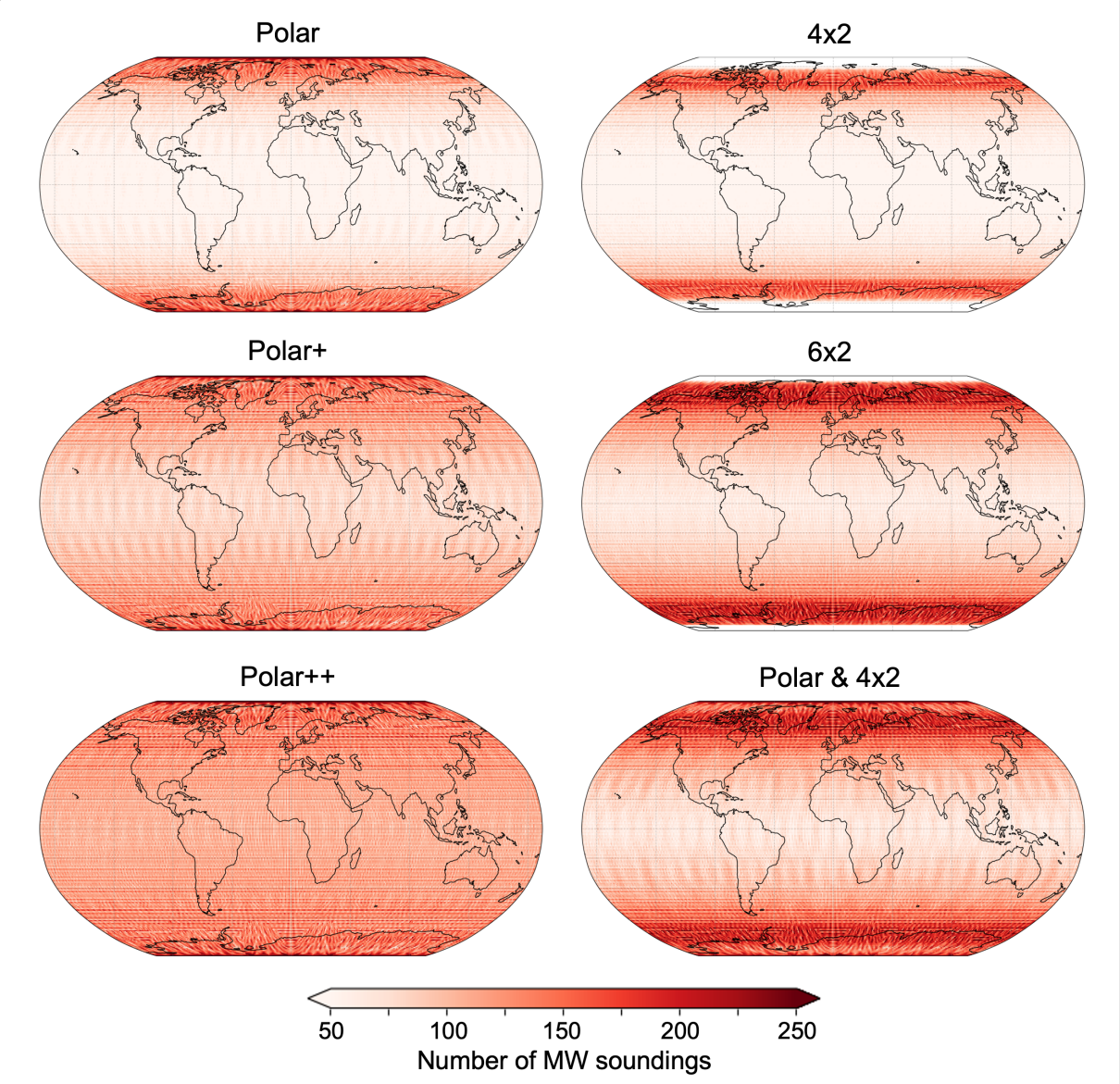

Figure 4: Maps showing the density of all simulated MW observation locations after thinning accumulated over two days (8-9 Jun 2018) for the six potential small satellite constellations tested (table 2).

error model that assigns larger observation errors in cloudy regions, based on a suitable indicator of the presence of clouds in the observations or the model fields (Geer and Bauer, 2011). To address this, a symmetric cloud indicator is defined which takes an average of the cloudy signals in the observation and the model. Further details and the mathematical formulation of the all-sky error model can be found in Appendix B. Inter-channel or spatial error correlations are not accounted for in the simulated data however, spatial thinning and assumed observation errors which are slightly inflated help to mitigate against this (similar to the treatment of AMSU-A and MHS).

For the existing MW temperature sounders, the symmetric cloud indicator includes use of low frequency channels that are not available on the small satellite. Therefore, a different cloud indicator is required for use on the small satellites for these channels. The alternative cloud indicator proposed for the small satellites measures the cloud effect in the window channel at 52.8-GHz (i.e. AMSU-A channel 4) and can be applied over both land and ocean surfaces. To test the effectiveness of the alternative indicator, parameters required for the all-sky error model were defined for AMSU-A and assimilation experiments run to ensure that the forecast impact of the all-sky use was adequately retained, accepting that we would not be able to perfectly replicate the performance of the current model. The experiments showed that while some small degradations are present in short-range forecasts such as the fit of lower tropospheric and humidity sounding channels on ATMS, the impact of the all-sky data can be well reproduced and impacts were neutral at medium ranges. Detailed discussion of the construction of the new indicator and the experimentation can be found in Lean et al. (2021b). Note that for the humidity sounding channels, the cloud indicator already in use for the existing sounders (based on a scattering index utilising channels at 89 and 150-GHz) can be applied to the small satellites so no adaptation is required.

Alongside the cloud indicators defined for the small satellites, the observation error model also requires input values of the minimum clear sky error and maximum saturated cloudy error for each channel. The parameters used in the observation error model for the new satellite data are based on values assigned for real data, but adjusted to account for different levels of instrument noise, as outlined further in appendix C.

4.5 Realism of brightness temperatures

In addition to the perturbations that have been explicitly added, variability will also be introduced through the differences in resolution and IFS versions used during the simulation and assimilation. We would ideally like to replicate a similar distribution of differences in simulated observations and short-range forecast (background departure statistics) that we would typically find with real observations. An important characteristic for use in the all sky framework is that the standard deviation of O-B should increase in the presence of cloud in the observations or model.

Figure 5 considers the dependence of the standard deviation of background departures on the indicator of cloud which forms the basis of the all sky observation error model (52.8GHz channel and a scattering index for the temperature and humidity sounding channels respectively). The standard deviation of O-B increases in the presence of cloud for both temperature and humidity channels as required. There is good agreement between the simulated and real data although some evidence of underestimation for the humidity channels in situations with higher cloud presence. Overall, the departure characteristics are considered to adequately replicate those of real observations.

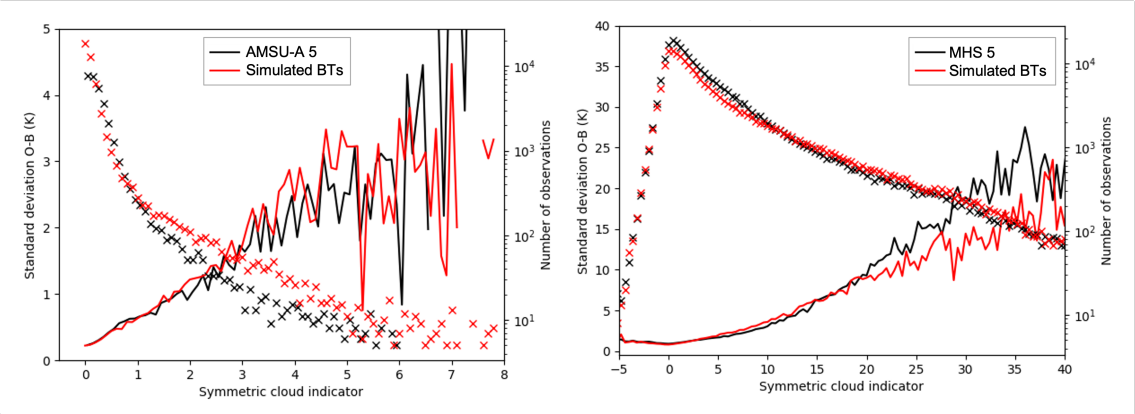

Figure 5: Increase in standard deviation of O-B (solid lines) with increasing presence of cloud signal for real AMSU-A channel 5 data (black) and simulated small satellite data for the equivalent channel (red) over land only (left panel). Right panel as right but showing MHS and equivalent simulated BTs over ocean only. Low values of the cloud indicator indicate clear-sky regions, whereas increasing values indicate increasing presence of cloud signals. Crosses indicate the number of observations (right y-axis). Data are from the period 9-14 June 2018 and from latitudes between 60°N-60°S.

4.6 Assimilation

After the simulated BTs have been produced, thinned, perturbed and have their accompanying observation error model defined, they are now ready for assimilation. Channels on the small satellites follow the same processing as equivalent channels on e.g. AMSU-A/MHS. More complete details of the all-sky treatment of temperature and humidity sounding instruments in assimilation can be found in Duncan et al. (2022) and Geer et al. (2022) respectively. A few of the key quality control and processing choices have been reproduced in table 4 which are applied to the assimilation of both the simulated small satellite data and existing MW data in the EDA experiments presented here. Choices include, for example, rejecting some channels with high surface sensitivity over difficult snow/sea-ice surfaces.

The current simulation of the new observations does not include the addition of any systematic errors, arising, for instance from errors in the calibration or the radiative transfer. Such biases are removed as part of the assimilation through variational bias correction (VarBC) (Auligné et al., 2007), and including such biases in the generation of the simulated data is hence not considered essential. However, it is important to avoid that the assimilation system treats the simulated observations as anchor observations, i.e. observations that are assimilated without bias correction and hence inform the bias correction of other observations. Therefore, we activate the use of VarBC for the observations from small satellites, allowing for a separate bias correction for each instrument and channel consistent with the treatment of all other sounding data. Adjustments to the small satellite data through the bias correction scheme remain stable and small in magnitude compared to those applied to real MW data (not shown) as required.

The handling of biases in the small satellite observations is a limitation in our current approach and could be revisited in future work. Nevertheless, the approach is equivalent to assuming that in the mean over all instruments the bias in the new satellite constellation is small, a situation that is broadly consistent with the experience from existing sensors. It is also worth noting that in any case the EDA is designed to estimate random forecast errors, and the influence of systematic errors in the EDA is a subject of ongoing research.

Table 4: Summary of key quality control and processing choices made in the assimilation of MW radiances on both small satellites and existing MW sounders

Assimilation choice	Application to all-sky MW
Radiative transfer model	RTTOV-SCATT v13 (Saunders et al., 2020; Geer, 2021)
Ocean emissivity	FASTEM-6 (Kazumori and English, 2015)
Land/sea ice emissivity	Dynamic retrieval using 50.3GHz for temperature sounding, 150GHz for humidity sounding (Karbou et al., 2006; Baordo and Geer, 2016)
Tropics (<30° N/S) orography rejection	53.596±0.115GHz height < 1000m, 54.4GHz height < 2000m
Extratropics orography rejection	53.596±0.115GHz height < 500m, 54.4GHz height < 1500m
Polar regions (>60° N/S)	183±7 and 183±4.5 rejected over all surfaces, 53.596±0.115GHz rejected over land/sea ice in Antarctic region only
Coast	53.596±0.115GHz, 54.4GHz, 183±7 and 183±4.5 rejected
Snow/sea-ice	183±7 and 183±4.5 rejected
Surface sensitive channel rejection	50.3, 52.8, 89, 157-GHz not directly assimilated (but used e.g. in emissivity and observation error calculation)

5 EDA spread results

Figure 6 summarises some of the key results from studying the EDA spread changes across all experiments using both real and simulated MW data. Here the EDA spread reductions for geopotential height at 500hPa are plotted against the number of sounding locations assimilated (i.e. a total representing the number of locations where one or more channels was used in the assimilation). The 500 hPa geopotential height is a key performance indicator in forecast impact assessment for the extra-tropics, and it is shown here for both hemispheres. The reference zero line is the baseline with no MW sounding data. Pertinent to the design of the small satellite constellation, figure 6 illustrates the following points:

- There is significant benefit from additional MW sounding observations over the range of constellations investigated compared to the Metop/JPSS baseline to which these constellations have been added. The smooth extension, particularly in the extra-tropics, in the trend of EDA spread reduction from the points using real MW data only (first three points) to the scenarios with additional simulated data lends further confidence to the simulation and EDA strategy.
- Even the smallest constellations considered (the 8-satellite Polar and 4x2 constellations) show a significant reduction in EDA spread. The magnitude of the spread reduction compared to the Metop/JPSS baseline is larger than the spread reduction resulting from adding MW sounders from Metop and JPSS to the no sounder baseline. Duncan et al. (2021) demonstrated that this would equate to a large positive impact in OSE experimentation.
- There is significant added benefit from the addition of the temperature sounding channels (black data points) compared to a humidity only selection (red points). This underlines the value of the more complex instrument design to accommodate these channels.
- There is evidence that the additional benefit from further MW soundings slows once the number

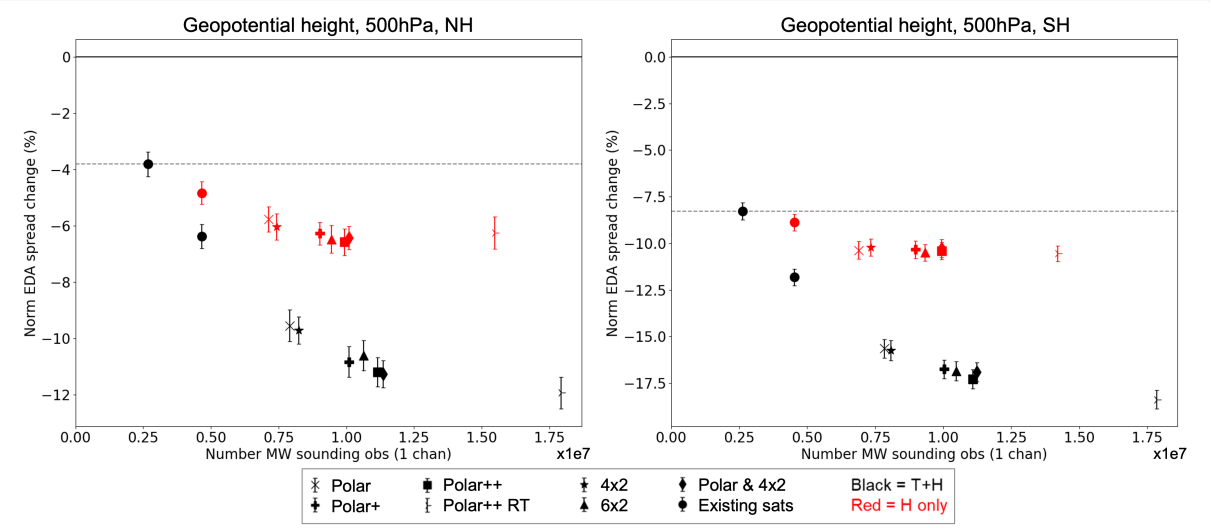

Figure 6: Percentage EDA spread reductions with increasing observation numbers for geopotential height at 500hPa from a baseline with no MW sounder data for all constellation options and baselines. Black and red symbols indicate respectively the addition of temperature and humidity sounding channels or humidity channels only to the Metop/JPSS baseline. Different symbols denote the different simulated data scenarios or use of real MW data. The additional "Polar++ RT" refers to a reduced thinning sensitivity experiment (see section 5.2). The point furthest left, picked out on the dotted grey line, corresponds to the Metop/JPSS baseline to which all other combinations of real and simulated data are added. Data are from the northern hemisphere (latitude $> 20°$N, left panel) and southern hemisphere (latitude $> 20°$S, right panel) over the period 8-28 June 2018. Error bars indicate an estimate of 95% confidence.

of observations approaches the higher end of the range tested, particularly for the constellations with humidity sounding only.

Figure 6 also highlights different magnitudes of spread reductions in different geographical regions where there are larger impacts in the southern hemisphere. Larger impact of satellite data in the southern hemisphere is commonly seen in OSEs and is often a consequence of the poorer coverage of conventional observations compared to the northern hemisphere. Different behaviour is also seen in the extra-tropics and tropics as illustrated using the temperature and humidity examples in figure 7 (note that impacts in the tropics can be less reliable due to sensitivity to changes to the mean errors). The reduction in EDA spread is generally smaller across the different variables in the tropics however, there is also a smaller number of observations. However, error growth in the tropics is very different from that in the extra-tropics, so a direct comparison is not meaningful. Figure 7 also shows that the rate at which the spread decreases with number of observations appears to be slower in the tropics, which is particularly noticeable when comparing experiments using temperature sounding channels (black points) in both areas. There is also a smaller difference in impact through the additional temperature sounding capability in the tropics. For geopotential height, wind and temperature, the combination of temperature and humidity channels is around 2-3 and 1.5-2 times larger than humidity only in the extra-tropics and tropics respectively compared to the Metop/JPSS reference. For the impact on humidity, these ratios are slightly smaller, suggesting that it may be more difficult to infer humidity changes indirectly through physical relationships with additional temperature information.

There is also significant impact on wind from adding MW sounding data, as can be seen in Fig. 8. This

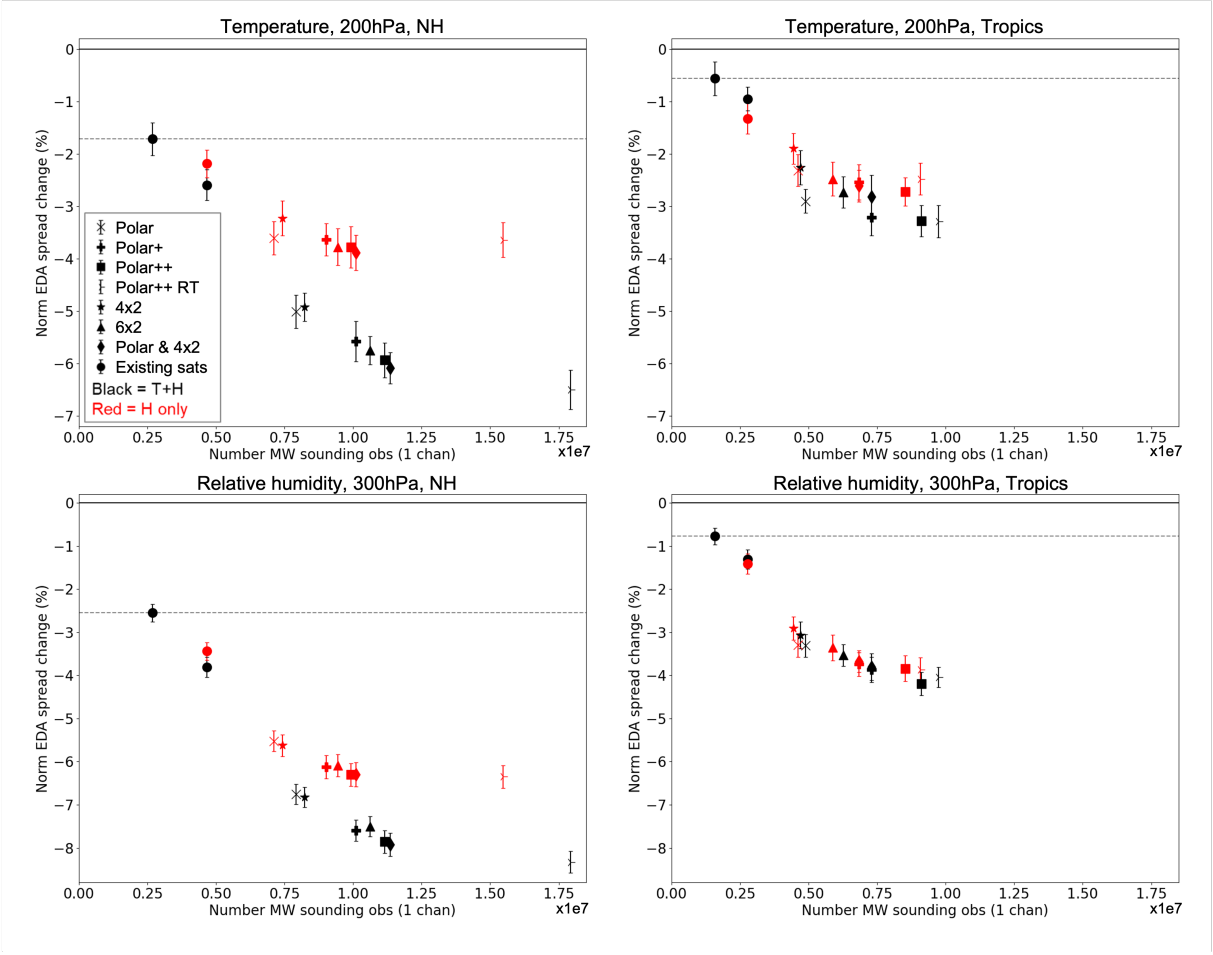

Figure 7: As for figure 6 but for temperature at 200hPa (top row) and humidity at 300hPa (bottom row) in the northern hemisphere (latitude $> 20°$N) (left panel) and tropics ($20°$S $<$ latitude $< 20°$N) (right panel).

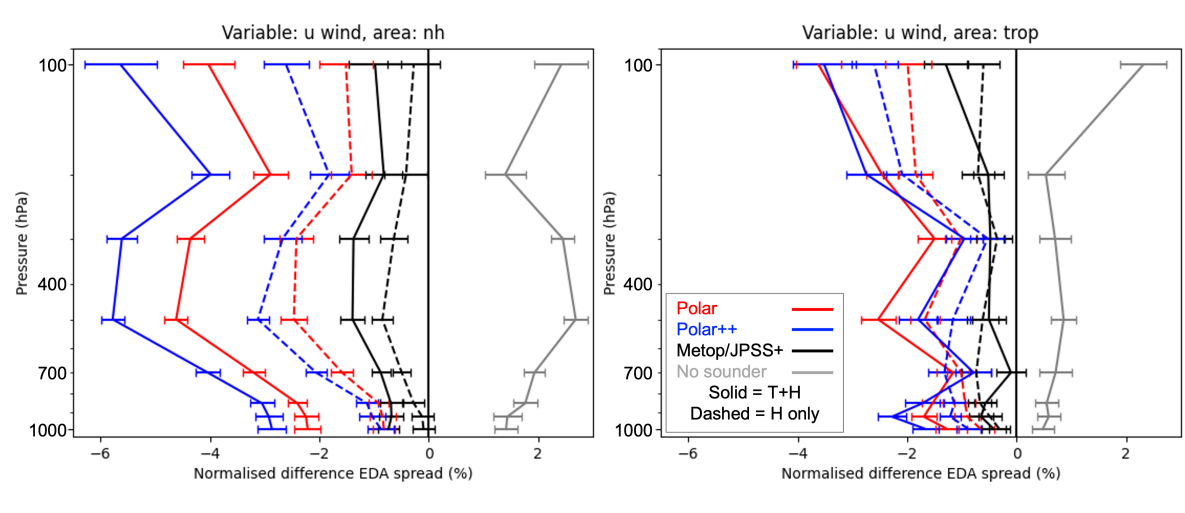

Figure 8: Vertical profiles of tropospheric EDA spread reduction for the U component of wind for a selection of scenarios (containing only sun synchronous MW sounding platforms) relative to the Metop/JPSS baseline. Solid and dashed lines indicate where both temperature and humidity or humidity channels only respectively have been added. Data are for the northern hemisphere (latitude $> 20°$N) (left panel) and tropics ($20°$S $<$ latitude $< 20°$N) (right panel) for the period 8-28 June 2018.

is inferred via balance relationships as well as from the ability of 4D-Var to derive wind information from the temporal evolution of humidity or cloud features. The latter is also known as "4D-Var tracing". Different mechanisms are responsible for changes in the importance of temperature or humidity information in the tropics and extra-tropics, and this is captured in the EDA results (Fig. 8): in the tropics, the dominant source of wind information is from the humidity tracing hence the additional temperature sounding channels have little extra impact. However, in the extra-tropics, geostrophic balance has more influence and therefore temperature information becomes more beneficial leading to the larger gap between channel sets in figure 8 (left panel). The experiments with simulated data (red and blue lines) show reassuringly consistent behaviour to the patterns with real data (black lines).

Results discussed so far have demonstrated the clear reductions in EDA spread in the troposphere however, there are also impacts extending into the stratosphere. Figure 9 shows an illustrative example of the changes in the stratosphere. Within the small satellite frequency selection, the highest peaking temperature sounding channel has most sensitivity around 80hPa. However, the weighting functions of microwave channels are relatively broad so there is still significant stratospheric sensitivity from this channel. Combined with the cycling nature of the assimilation system which can propagate changes vertically from higher pressures, EDA spread reductions are achieved even at very low pressures. Figure 9 also shows the gap in spread reduction between the real (solid black line) and simulated data (solid blue and red lines) experiments using both temperature and humidity channels becomes smaller in the stratosphere. This reflects the benefit from having more direct stratospheric sampling from additional temperature channels on the real MW instruments.

5.1 Observation distribution

So far, the results have addressed the EDA spread change with increasing total observation number but there is spatial variation of the density of observations for the different potential constellations (figure

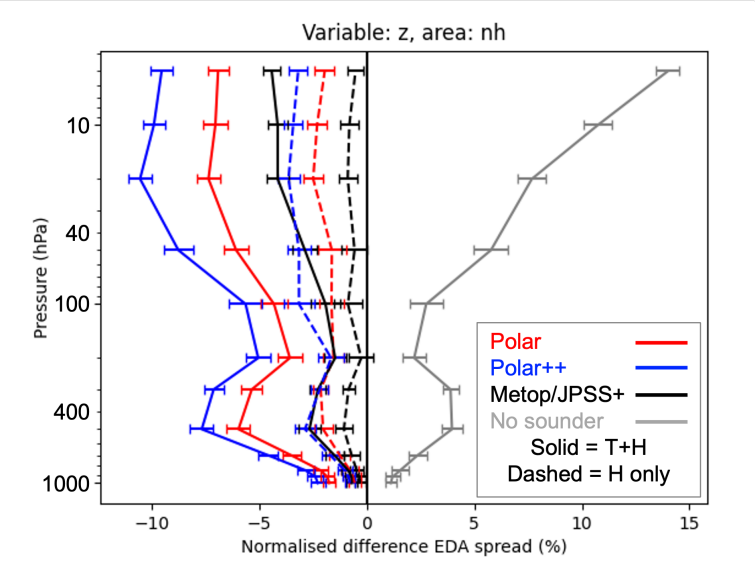

Figure 9: As for figure 8 with extension into the stratosphere and showing geopotential height for the northern hemisphere (latitude $> 20°$N).

4). The interaction between the satellite phasing and thinning (discussed in section 4.2) means that in the polar regions (>60°), scenarios with the inclined orbits hence show a higher total of observations than purely polar orbiting scenarios despite having fewer satellites. This is also the reason why the number of used soundings shown e.g. in Fig. 6 do not increase as much as might be expected given the number of satellites involved in each constellation. When looking at spread changes in the extra-tropics and polar regions, the values for the inclined orbits may be more dominated by the 60-75°N/S bands. A sensitivity experiment to address the effect of thinning data from different satellites together for the Polar++ constellation is presented in the next section.

The effect of the different geographical distribution of the observations has been investigated in more detail for the Polar and 4x2 scenarios which use the same number of satellites but in different orbit configurations. By building on a baseline system of Metop/JPSS satellites, the backbone constellation provides the continued direct sampling of the polar regions in the inclined orbit scenarios. However, additional EDA spread reduction is seen from the extra direct measurement in the Polar scenario in the polar regions, particularly visible in the Antarctic, as illustrated in the example in figure 10. Where observations are densest for the inclined orbits, there are some larger spread reductions visible around 70°S but the difference is less clear in the northern hemisphere. Satellites tend to have greater impact in the southern hemisphere where there are fewer conventional observations so the difference between the two scenarios may be more amplified here. The EDA spread in northern hemisphere storm track region (30-60°N) also shows no significant difference between the Polar or 4x2 constellations. The highest densities of the inclined orbits are further north than the storm track region so to see more benefit at these latitudes, a lower inclination orbit may be required. Also worth noting is that the Polar scenario appears to perform better in the tropical region compared to the 4x2 constellation, likely reflecting the greater observation numbers used over the tropics for the Polar scenario. To achieve better coverage over the tropics, an inclination of 30-40° is likely required.

The Polar & 4x2 constellation was chosen to investigate whether a different distribution of satellites could achieve similar results as a larger constellation made up of the same orbit type such as Polar++.

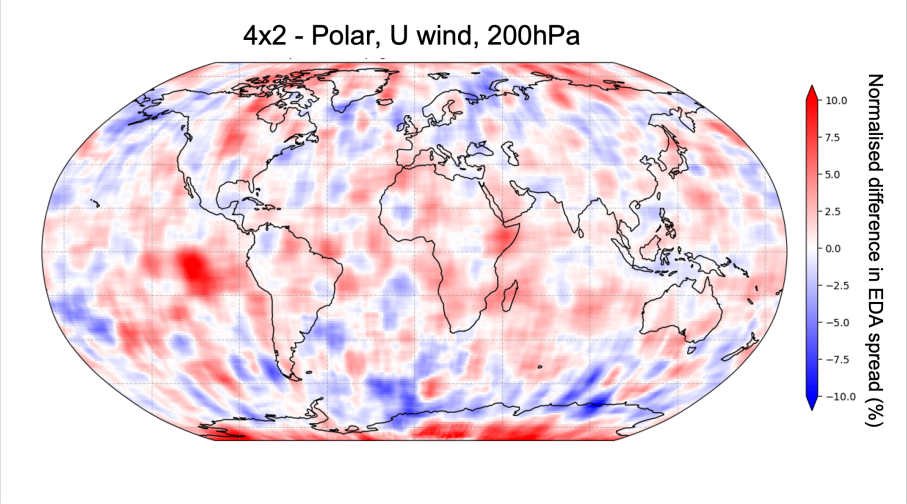

Figure 10: Map showing the percentage difference in EDA spread between the Polar and 4x2 constellations. Bluer colours indicate areas where a greater spread reduction is seen in the 4x2 scenario.

Considering the suboptimal interaction between the phasing and thinning for the polar orbits, which becomes increasingly important for the larger constellations, it is difficult to draw conclusions about the advantage of fewer satellites in a mix of orbits. In the extra-tropics, results show that the Polar & 4x2 constellation is able to achieve similar EDA impacts as the Polar++ with the suboptimal thinning. Conversely, as the polar orbits have slightly higher data coverage in the tropics (which is less affected by the phasing/thinning interaction), similar numbers of observations are achieved through the Polar+ scenario with two fewer satellites while the EDA impact is similar. A mixture of polar satellites with inclined orbits focusing more on the tropical regions might provide more contrast in coverage to the polar only option.

5.2 Sensitivity to thinning

To investigate the effects of a much higher density of observations, a sensitivity test was performed where the Polar++ EDA experiments were repeated but with spatial thinning only applied to individual satellites and not to all the satellites together. By comparing the new coverage for this reduced thinning (figure 11) with the original Polar++ observation density (figure 4) it is clear that there is a vast increase in the data that is assimilated in the polar regions. As there is little overlap between satellites in the tropics, the density here remains similar. Figure 6 showed earlier that these experiments provide the extreme high number of MW sounding locations but the effects of the thinning change can be most acutely seen by focusing on the polar regions. Figure 12 shows the EDA spread changes comparing the north/south pole regions. A less extreme point is seen for the south pole in the humidity only experiment due to screening of the humidity channels over the Antarctic land area.

By design, any additional data in the Polar++ RT case is due to several satellites observing a similar location at approximately the same time, rather than through better temporal sampling. This means the benefit of these observations arises only from reducing the effective observation noise, rather than through better observation of fast evolving weather systems. When the temperature sounding channels are included, the effective noise reduction still leads to some benefit (compare the Polar++ and Polar++ RT points in Fig. 6), as we are noise-limited for these channels, though the rate has slowed significantly.

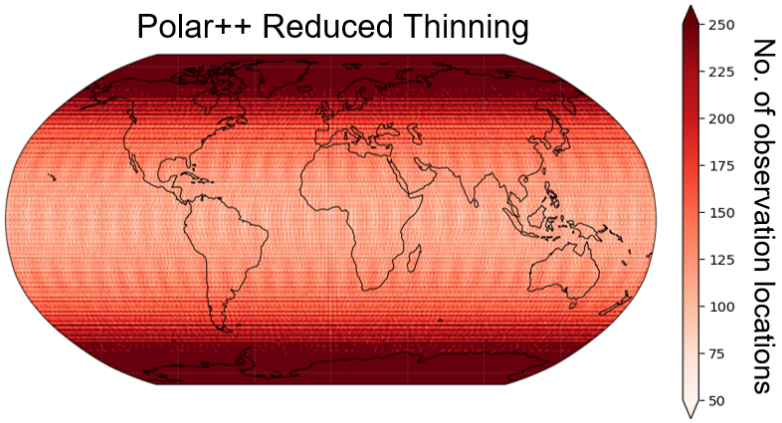

Figure 11: Map showing the density of all simulated MW observation locations accumulated over two days (8-9 Jun 2018) for the Polar++ constellation where spatial thinning has been applied to individual small satellites rather than thinning all satellites together.

In contrast, the benefit for including only the humidity sounding experiments has plateaued at these high numbers, as the instrument noise is not a limiting factor and repetitive observations at the same location have hence little additional benefit. Note that these experiments do not explicitly account for spatial or temporal error correlations, arising, for instance from representation error, and these may become more relevant for the large data densities. The effect of neglecting such error correlations is not clear for these experiments, but it is likely that the spread reductions obtained for the Polar++ RT case are optimistic, unless such error correlations are accounted for in the assimilation. In any case, a better phasing of the Polar++ satellites, optimised for temporal sampling, may achieve better results than what is obtained here, with or without the reduced thinning, via the added benefit of observing fast-evolving weather systems.

6 Conclusions and further work

Microwave temperature and humidity sounding data from satellites currently provide a significant positive impact on NWP and continued improvements to the forecast from adding the latest instruments suggests that even more benefit could be obtained with further additional instruments. With recent technology advances, a constellation of small satellites could allow a cost-effective solution to providing such higher temporal coverage, provided the data quality is adequate for NWP. An optimally designed future constellation of small satellites carrying microwave sounders will have to balance the benefit to NWP against practicalities such as cost and instrument limitations. In this study, the key design aspects considered are the number of satellites, their orbit types, and the relative benefits of the MW instrument having humidity and temperature sounding capabilities versus humidity sounding only.

A selection of six potential constellations were chosen for evaluation which span a range of satellite numbers and different orbit combinations. Each small satellite constellation was tested with 183-GHz humidity sounding channels, alongside two window channels, and with additional temperature sounding channels in the 50-GHz band, with channel characteristics based on sub-sets of channels chosen for the instrument on the Arctic Weather Satellite. When testing the value of humidity sounding channels,

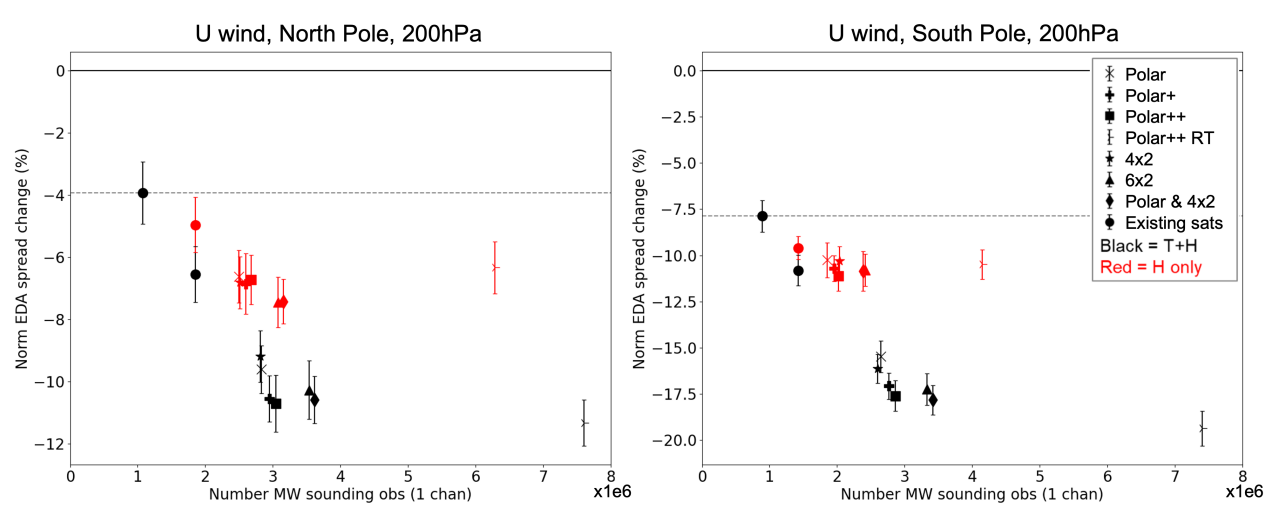

Figure 12: As for figure 6 but for U wind at 200hPa in the north polar (latitude $> 60°$N) (left panel) and south pole (latitude $< 60°$S) (right panel).

their successful assimilation is reliant on accompanying window channels around 89-GHz and 165-GHz which provide critical information on emissivity and cloud amount in the observation error model. Therefore, when the value of the humidity channels is discussed, it should be noted that this implies the additional presence of these essential window channels. BTs were simulated for each constellation and a corresponding observation error model defined. The simulation of the data followed as closely as possible the same processing applied to the real MW data. The resulting BTs showed a good degree of realism in background departure statistics when subsequently ingested in a lower resolution 4D-Var experiment. An EDA approach was used to investigate the relative impact of each constellation, added to a baseline of real observations with four MW sounders in the Metop/JPSS orbits providing a conservative backbone of the existing MW sounders alongside an otherwise full observing system. The key measure analysed was the change in the reduction of EDA spread, which equates to improving the forecast uncertainties.

The key conclusions from the EDA spread analysis are:

- The temperature sounding capabilities produce a significant additional EDA spread reduction across a range of variables. In the extra-tropics and tropics, this is in general of the order 2-3 and 1.5-2 times greater respectively than the EDA spread reduction from humidity-sounding channels only across the different pressures and variables considered. Temperature sounding channels in the 50-GHz band would therefore be a worthwhile addition where they can be sensibly accommodated on a future small satellite.

- The smallest constellations of small satellites, eight satellites either in polar orbits or mid-inclination orbits, show a very significant reduction in EDA spread, more than doubling the impact of the four MW sounders already present in the baseline used. It is encouraging that an impact of this magnitude can be accomplished with a relatively small number of platforms.

- Continued reduction in EDA spread is seen with adding more observations but the rate of reduction slows. The humidity only experiments show more evidence of the benefit becoming harder to extract with greater numbers of observations.

- There is clear benefit for wind from the additional MW sounding observations. In the tropics, this stems largely from the humidity sounding channels via the 4D-Var tracing effect, whereas in the extra-tropics the additional temperature sounding channels play the larger role, as geostrophic balance becomes more important.

The present results suggest that significant forecast benefits can be achieved from a MW sounding constellation that complements a backbone of MW sounders. The results highlight that most of this benefit can be achieved with a constellation of relatively modest size (8 satellites added to a 4-satellite baseline), where the EDA spread change is comparable to or larger than the impact of adding the four MW sounders on the Metop/JPSS satellites to a baseline with no MW sounding data. Experimentation with real data suggests that such a change should result in a significant improvement in OSEs. Meanwhile, the benefit of even more satellites gradually diminishes and may not be cost-effective. The study also highlights that the relative phasing of the satellites combined with current ad-hoc thinning practices strongly affect the amount of data assimilated, and further optimisations in the use of the data may be required in this respect, particularly for large constellations. Note that our study assumes that high-performance MW sounding observations continue to be available as part of the backbone constellation, and these are still considered essential. They provide reliable high-accuracy observations needed for cross-calibration and long-term climate records. Furthermore, they provide mid- to upper stratosphere information as well as low-frequency channels which cannot be easily accommodated on small satellites. Given the finding that most of the impact can be achieved with the smallest constellations considered, it would be beneficial to further investigate how a cost-effective smaller constellation could be optimised (e.g., in terms of the number of satellites, orbital planes, etc). Such work will be conducted in the context of the Arctic Weather Satellite Constellation as part of a EUMETSAT-funded study.

The relative behaviour of the EDA spread reduction as a function of the number of observations for the two channel sets considered is an interesting result of this study and warrants further discussion. Given shorter time-scales for humidity, there may have been expectation that improved temporal sampling would be particularly beneficial for humidity. While the benefit of additional humidity-observations is clear, the rate of benefit appears to slow considerably in the case of the humidity-only scenarios. While this may indicate real diminishing benefits from extra humidity-information, there are also reasons to suggest that our simulations may under-estimate the impact of humidity-observations. For instance, even though the observations were simulated from high-resolution analyses, these will still be smoother than reality. This aspect is likely particularly relevant for humidity sounding observations, and will, for instance, affect 4D-Var's ability to infer wind information from the evolution of humidity or cloud structures. Also, representation error plays a larger role for humidity sounding channels, and the treatment of this could be further advanced, both in the simulations as well as in the assimilation of real data. The continued clear benefit from additionally assimilating temperature sounding observations in contrast may largely reflect that observing capabilities are noise-limited for temperature sounding, hence there is benefit from reducing the effective noise through additional observations. Additionally, at the resolution (T_L255) at which the EDA spread is calculated (corresponding to the highest 4D-Var minimisation resolution), changes in the fast evolving, small scale processes associated with humidity may not be as well captured as the larger scale structures impacted by the effective noise reduction in temperature observations. A further study could explore the resolution dependency of the relative EDA spread changes for the different channel sets, particularly as the minimisation resolution is expected to increase in the future. As the temperature-channels are added to the humidity sounding channels, there may also be synergistic benefits from having both types of information available, resolving geophysical ambiguities in the radiances. These aspects could be studied further, for instance by adding temperature sounding channels only, or by investigating the sensitivity of the results to the noise-specification, particularly for the temperature sounding channels.

No clear advantage is found for a particular distribution of the satellites in the different orbit types considered here although there is evidence that the polar regions benefit more from direct observation as provided by the constellations with sun-synchronous orbits. The polar constellations are however disadvantaged due to the set up of the phasing of the satellites where duplication of coverage in the high latitudes has not been minimised. This leads to a suboptimal interaction with the thinning that results in a disproportionate loss of data in the polar regions for the assimilation. The two constellations with eight satellites (Polar and 4x2) show very similar results while the Polar & 4x2 combination with 16 small satellites shows similar impacts to the larger Polar++, 20 satellite constellation. Adapting the phasing to have similar revisit and global coverage times but built-up using orbits with less overlap would be useful to make a fairer comparison. The relative phasing between satellites in different orbital planes is expected to be more optimised in this respect for the planned EDA-evaluation of the Arctic Weather Satellite Constellation. As a separate future extension, it would also be interesting to consider a combination of polar orbits with satellites in an even lower inclined orbit (e.g., 30-40° inclination), to address the temporal coverage in the tropics.

EDA experiments with changes to real MW data also provided the opportunity to investigate the correspondence to impacts in traditional OSEs. While there is clear evidence that EDA spread changes are a useful indicator of changes in short-range forecast skill, the under-spread nature of the EDA means that a simple one-to-one relationship is not applicable. In this context, it is also reassuring to see that EDA spread reductions obtained with simulated data generally show a smooth continuation of trends and vertical structure seen in the spread reductions found for real data, advising further confidence in the results for the spread reductions. The interaction of the phasing and thinning highlights the sensitivity of these EDA experiments to practical assumptions that must be taken in the data processing. Is it also a reminder that more generally, the relative importance of different components found in this study are dependent on the current MW assimilation scheme, including e.g. the thinning strategy, treatment of error correlations or use over complex surfaces. Further advances in the use of MW sounding data, or indeed in the general assimilation system or the global observing system will hence affect the impact that will be achieved in the future.

There are some caveats that should be kept in mind when interpreting the results of this study. We have assumed that random and systematic observational errors for the small satellite data are in line with those of present observations, taking only into account differences in the instrument noise. While the instrument noise estimates used are considered realistic for a small satellite concept, it remains to be established that other sources of error for the small satellite data are indeed in line with those we are currently used to. This is particularly true for calibration-related biases, for which our study assumes that they can be successfully corrected using current bias correction methods. If this is not the case, it is hoped that adequate corrections can be developed, aided by the continued presence of a backbone of reference-like MW sounding instruments.

Acknowledgements

The authors would like to thank members of the ESA partner project (comprising a consortium of JCR Systems Ltd, Informus GmbH, In-Space Missions Ltd and Fluctus SAS) who provided the orbital parameter files needed for the observation simulation in addition to their expertise on viable constellations. The authors would also like to thank Elias Hòlm and Katrin Lonitz for discussion on the EDA and Alan Geer and David Duncan for providing technical support and information, particularly around MW processing aspects in the IFS code.

Appendix A Considerations for 3x3 averaging

The sample instrument noise values for the small satellite data considered in this study are typically around 0.6 K for the tropospheric temperature sounding channels (Table 3), which is relatively large compared to errors in short-range forecast equivalents that are typically of the order of 0.1 K. At the same time, the data are strongly oversampled, with sampling at around 10 km at nadir for 40 km footprints. The situation is similar to that of ATMS, for which data are hence super-obed to reduce the effective noise for the temperature sounding channels prior to assimilation, down to values more in line with those for typical forecast errors. For ATMS, nine FOVs are averaged across three neighbouring scan positions and scan lines (Bormann et al., 2013).

An analysis of the noise reduction, the resulting FOV size, and the spatial sampling of different averaging choices revealed that a 3x3 averaging pattern is also found to be practical here for the small satellites. For simplicity, only pattern that average over the same number of scan-lines and scan-positions were considered. To achieve a noise performance that is in line with heritage instruments such as AMSU-A and more comparable to typical short-range forecast errors, an averaging of 3x3 or 4x4 would be required. In the case of uncorrelated noise, this leads to effective sampling noise values for the tropospheric temperature sounding channels of around 0.2 K or 0.15 K, respectively. The reduction in noise through spatial averaging of course needs to be traded off against the degradation of the effective FOV size and the spatial sampling. Resulting effective FOV sizes at nadir are evaluated in Figure 13 and 14. For temperature sounding channels, both 3x3 and 4x4 averaging applied to the small satellite produce similar effective FOV sizes to ATMS and AMSU-A at nadir. For the humidity sounding channel, 4x4 averaging compares more favourably with averaged ATMS data at nadir while 2x2 averaging (not shown) would better match the MHS FOV. However, at the scan edges the differences are more noticeable, as the lower orbit means that the effect on the cross-track FOV size and the spatial sampling are more severe. This is illustrated in Fig. 15 which highlights that for the temperature sounding channels the 3x3 averaging leads to a sampling at the scan-edge that is more comparable to AMSU-A or averaged ATMS for comparable cross-track distances. For this reason, the 3x3 averaging rather than 4x4 averaging was chosen for the small satellite data.

The choice of 3x3 averaging is applied consistently across all the frequencies on the small satellite. However, in practice, no averaging is performed on the simulated data but instead every third scan position and every third scan line is selected. This sub-selection hence also contributes to simulating representation error - differences in the model background and real MW observations will exhibit different representativeness of clouds and realistic simulated BTs should also have this characteristic.

Appendix B Outline of the all sky observation error model

The all sky error model increases the observation error in the presence of cloudy signals from either the observations or the model. This is to account for different representativeness of clouds in the observations and model. Larger observation errors are assigned in cloudy regions, based on a suitable indicator of the presence of clouds in the observations or the model fields (Geer and Bauer, 2011). Figure 16 shows a simple schematic of the formulation in terms of the cloud indicator.

The all-sky observation error is applied to all temperature and humidity sounding channels with sensitivity to the presence of clouds. Where temperature sounding channels have a peak sensitivity in the stratosphere, the impact of cloud is negligible so the error model becomes a constant value. For MW temperature sounding channels, different cloud indicators are used for AMSU-A data and the simulated

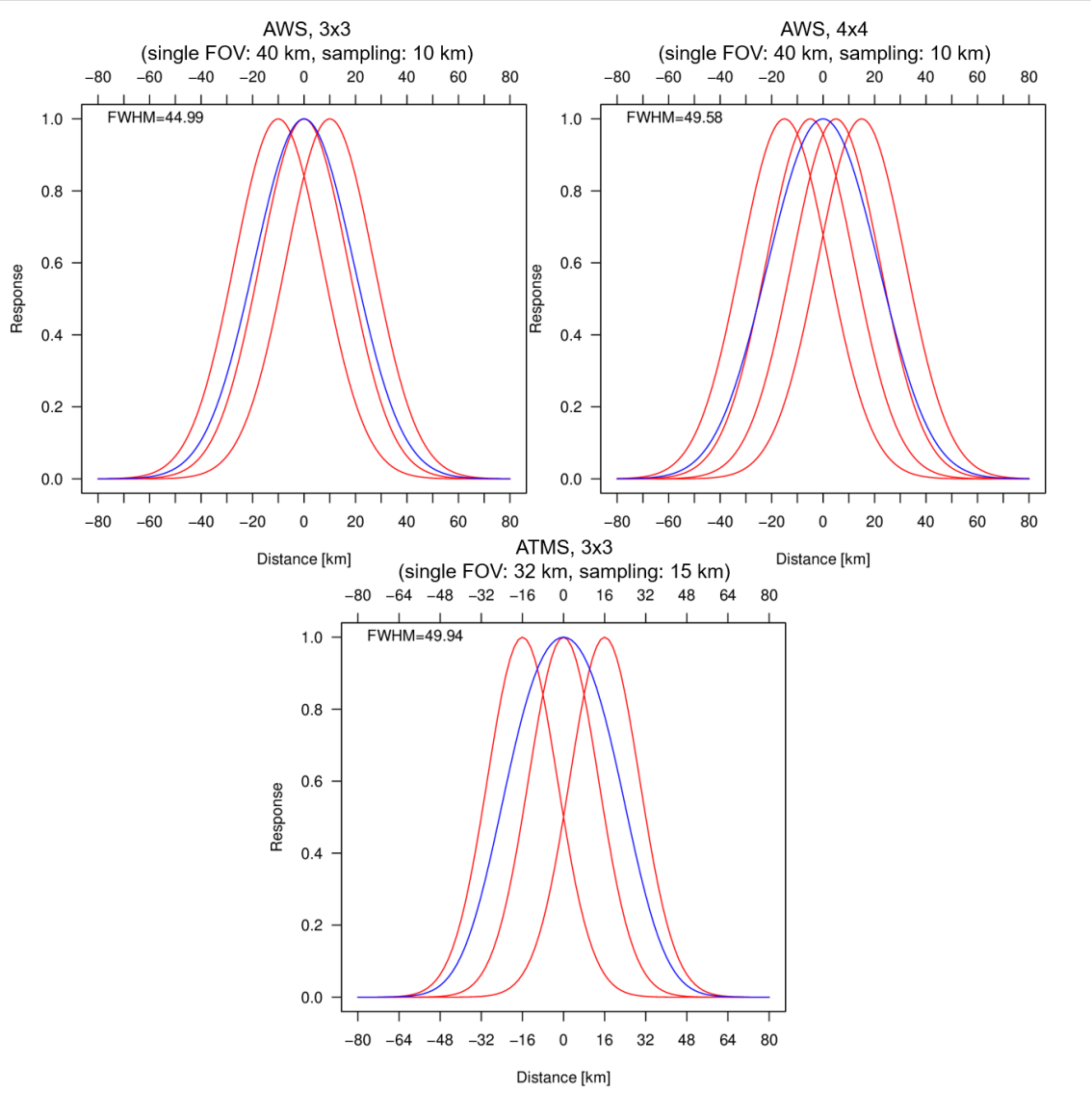

Figure 13: Point-spread-function (at nadir) for a temperature sounding channel for individual samples with 40 km FOV (red) and the average of the FOVs (blue) using a 3x3 and 4x4 averaging for an AWS-like instrument (top row) and the 3x3 averaging in place for ATMS (bottom row). The point-spread-function for raw samples is approximated here by a Gaussian with a Full Width at Half Maximum (FWHM) equal to the specified FOV size. For comparison, the FOV size for AMSU-A at nadir is 48 km. For each case, the FWHM value of the averaged FOV is indicated on the plot.

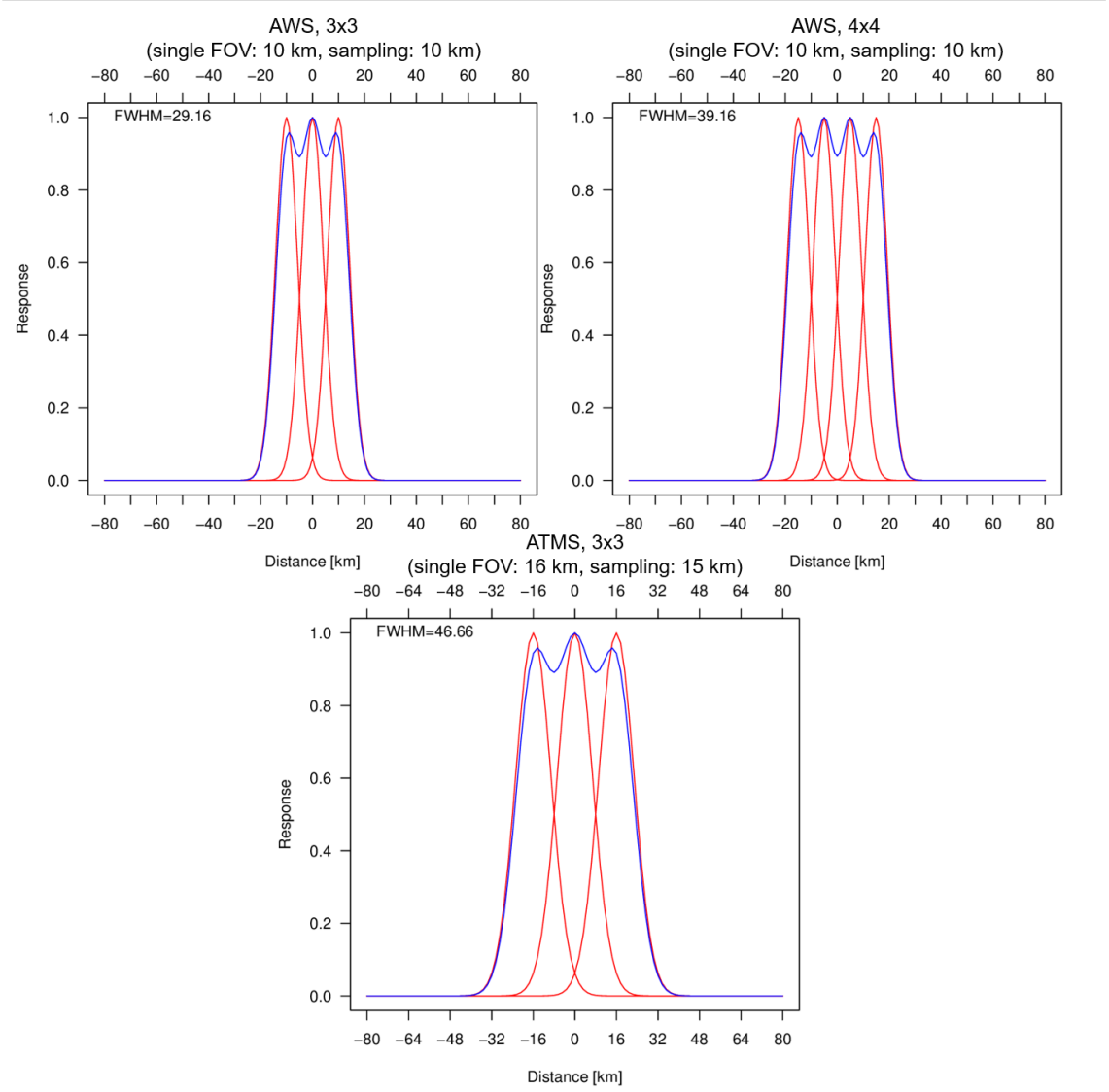

Figure 14: As for figure 13 but for the humidity sounding channels with FOV size 10km. For comparison, the FOV size of MHS at nadir is 16 km.

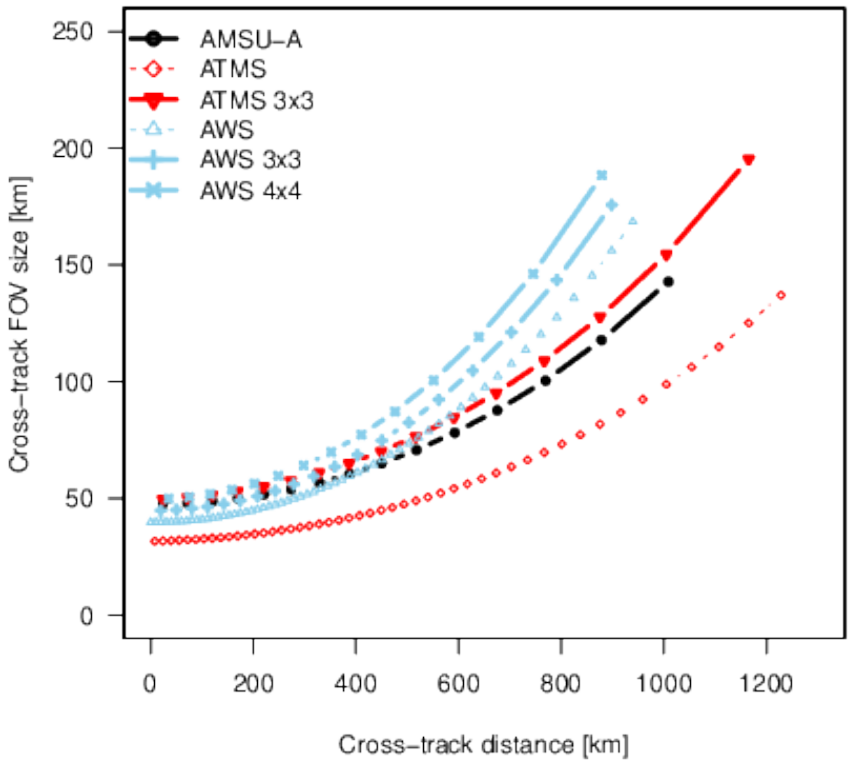

Figure 15: Approximate cross-track FOV sizes as a function of cross-track distance from nadir for temperature sounding channels on a range of sensors, before and after spatial averaging, as indicated in the legend. Values have been calculated from nadir-values using zenith angles applicable to typical satellite altitudes.

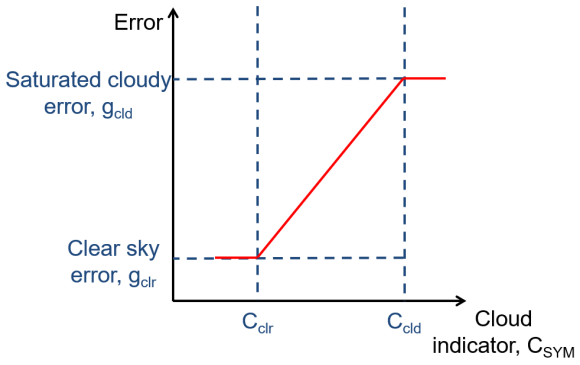

Figure 16: Simple schematic showing how the coefficients in equations 4 - 6 define the form of the error model.

small satellite data due to the availability, or not, of lower frequency channels. For AMSU-A, there are two different cloud indicators used in the error model corresponding to land or ocean surfaces. Over land, the difference 23.8-89GHz provides a scattering index which exploits the increased scattering from frozen hydrometeors at 89GHz compared to 23.8GHz (Bennartz et al., 2002). Over ocean, the indicator is the retrieved liquid water path (Grody et al., 2001) which is derived from 23.8GHz and 31.4GHz channels. For the small satellite data, an indicator based on the 52.8GHz channel which measures the cloud effect in a window channel is used over both land and sea (Lean et al., 2021b). Meanwhile, for humidity sounding channels around 183GHz, a scattering index utilises channels at 89GHz and 150GHz (Geer et al., 2014) (which both remain available in the small satellite configuration). Differences in scattering from precipitation-sized ice particles are exploited, similar to the land scattering index model for AMSU-A temperature sounding channels. This makes it very suited to the 183GHz channels where frozen particles dominate the scattering (Lui, 2008; Geer and Baordo, 2014).

The cloud indicator used in the error model is formulated by taking the average of the cloud indicator values for the observations and the model background:

$$C_{SYM} = (P_{obs} + P_{bkrd})/2 \tag{3}$$

Where P_{obs} is the indicator calculated using observed values e.g. the difference in observed brightness temperatures at 23.8 and 89-GHz for the scattering index and P_{bkrd} is calculated using the model background equivalent brightness temperatures. The final observation error is then constructed with either a linear or quadratic dependence on the cloud indicator as the following (reproduced in the linear form using the same notation from Geer et al. (2014)):

$$g_{clr} \in C_{SYM} <= C_{clr} \tag{4}$$

$$g(C_{SYM}) = g_{clr} + (g_{cld} - g_{clr}) \left(\frac{C_{SYM} - C_{clr}}{C_{cld} - C_{clr}} \right) \in C_{clr} < C_{SYM} < C_{cld} \tag{5}$$

$$g_{cld} \in C_{SYM} >= C_{cld} \tag{6}$$

Where g_{clr} and g_{cld} are the clear sky and saturated cloudy error values respectively while C_{clr} and C_{cld} are threshold values of the symmetric cloud indicator to separate clear and saturated cloudy situations,

respectively. The clear sky values reflect the individual channel noise estimates of the instrument, inflated in recognition of other error sources in this situation e.g. from forward modelling error. The cloudy saturation value and the choice of a linear or quadratic nature of the model are determined by analysing the standard deviation of background departures binned as a function of the symmetric cloud indicator. These values are determined separately for each satellite and individual instrument channels. Figure 16 illustrates how these parameters define the construction of the error model.

Appendix C Estimation of small satellite clear sky observation errors

Observation errors assigned in data assimilation describe different sources of error, typically classified into measurement error (such as instrument noise) and representation error. To devise the parameters for the observation error model outlined in appendix B, we assume that the representation error for the new data is the same as for the real data, but only the instrument noise is different. This is justified, given the similarity of the channels as well as the similarity of the footprint sizes. Note, however, that for real data we currently do not explicitly model the contributions from instrument noise and representation error separately in the observation error model. Instead, the parameters of the observation error model are set empirically, based on the standard deviation of background departures which provide an upper limit for the overall observation error in the absence of correlations between observation and background error. In order to separate out the contribution from instrument noise some reverse engineering is needed. The instrument noise only matters for the clear-sky parameter of the error model, as otherwise representation error dominates, so the following focusses only on the clear-sky parameter. For the cloudy observation error setting, we simply adopt the same values as used for real data, as sample NEDT is a negligible contribution.

To link the empirically assigned clear-sky observation error to the sample NEDT, we proceed as follows: we model our assigned (clear-sky) observation error $\sigma_{o,clr}$ as a combination of the instrument noise σ_{NEDT} and representation error σ_r, and a scaling factor a which accounts for other neglected effects in the error modelling, such as error correlations. Assuming that the two error contributions are uncorrelated, the relationship becomes:

$$\sigma_{o,clr} = a\sqrt{\sigma_{NEDT}^2 + \sigma_r^2} \tag{7}$$

The values for σ_r and a are derived from real data as follows: First, σ_r is derived by considering standard deviations of background departures and channel-specific sample NEDT values provided with the data. This makes use of the fact that we presently have several instruments available in the ECMWF system, with some variations in the instrument noise performance. For the temperature sounding channels, there is mostly a clear relationship reflecting that instrument noise is a dominant part of the error budget (e.g. figure 17, left). The relationship follows $\sqrt{\sigma_{NEDT}^2 + \sigma_r^2}$, with an appropriately fitted σ_r. Then, the scaling factor a is derived by considering assigned σ_o and sample NEDT values for real data. The relationship between these two quantities is not as clear (e.g. figure 17, right). This is primarily because instrument noise values have changed since the parameters of the observation error model have been derived some time ago, and the parameters have not been updated. The value a is chosen to nevertheless give the best overall fit, using the relationship given in equation 7 with σ_r derived previously. Separate parameters have been derived for land and sea, and the values are given in Table 5.

For the temperature sounding channels, the representation error derived in this way is typically relatively small, with values mostly around 0.1 K and hence smaller than the sample NEDT. In contrast, representa-

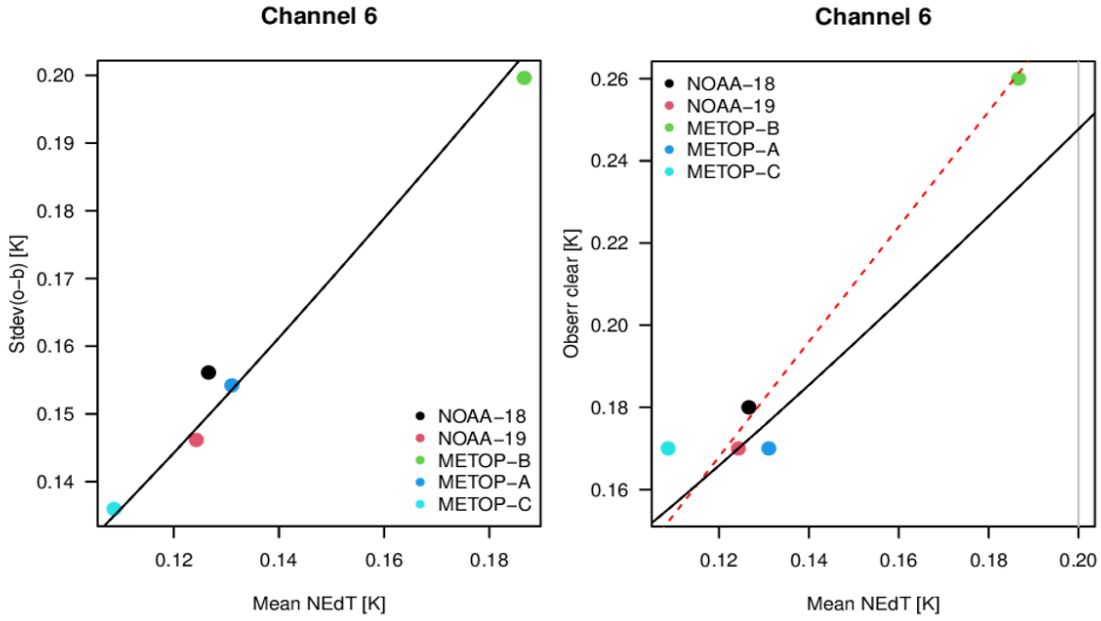

Figure 17: Standard deviation of O-B vs. sample NEDT (left) and assigned clear sky observation errors vs. sample NEDT (right) for AMSU-A channel 6 on various satellite platforms. Fitted lines show the results from using a simple scaling of sample NEDT (red dashed) or using equation 7 (solid black line). The grey line indicates the sample noise for the small satellite after 3x3 averaging. Data are from 13-31 May 2021.

tion errors for the humidity sounding channels are much larger, with values of 1.4-2.0 K and hence larger than the instrument noise. This reflects that representation error plays a much larger role for these channels, even in clear-sky regions. In fact, the observation error assignment for humidity sounding channels in the ECMWF system currently neglects different instrument noise values for different instruments, and instead assigns the same value. The scaling factors a tend to be similar for different temperature sounding channels, with values of around 1.15, whereas they tend to be slightly larger for the humidity sounding channels, with values up to 1.4.

The above derived relationships are used with the sample NEDT estimates (Table 3, divided by three to account for the 3x3 averaging) to obtain the clear-sky observation error values for the small satellite data. The resulting values for the temperature sounding channels are around 0.25-0.3K, which is slightly higher than AMSU-A equivalents. For the humidity sounding channels, the resulting values are very similar to those used for MHS. While primarily derived for the purpose of specifying observation error values for the present study, the derived relationships could also be considered in a refined observation error model in the ECMWF system that allows for changes in the NEDT of real data, as a result of instrument ageing and other effects.

References

Arnold, C. P., J., Dey, C.H., 1986. Observing-Systems Simulation Experiments: Past, Present, and Future. Bulletin of the American Meteorological Society 67, 687–695. doi:10.1175/1520-0477(1986)067<0687:OSSEPP>2.0.CO;2.

Table 5: Values of tuneable parameters (scaling factor a and "representation error" σ_r) to compute the clear sky observation error from the sample NEDT values for each channel. Statistics are based on considering departures from the ECMWF system over two seasons (13-31 May and 12-31 Oct 2021), as described in the main text.

AMSU-A/MHS channel	a	σ_r	a	σ_r
	sea		land	
AMSU-A 5	1.15	0.14	1.15	0.37
AMSU-A 6	1.15	0.08	1.15	0.13
AMSU-A 7	1.15	0.08	1.15	0.08
AMSU-A 8	1.15	0.08	1.15	0.08
AMSU-A 9	1.15	0.09	1.15	0.09
MHS 3	1.30	1.4	1.3	1.45
MHS 4	1.25	1.5	1.3	1.35
MHS 5	1.10	1.95	1.4	1.4

Atkinson, N., 2015. NE△T specification and monitoring for microwave sounders. NWP SAF Technical Report, version 1.1 Doc ID: NWPSAF-MO-TR-033, 12pp.

Auligné, T., McNally, A.P., Dee, D.P., 2007. Adaptive bias correction for satellite data in a numerical weather prediction system. Q.J.R.M.S. 133, 631–642. doi:https://doi.org/10.1002/qj.56.

Baordo, F., Geer, A., 2016. Assimilation of SSMIS humidity-sounding channels in all-sky conditions over land using a dynamic emissivity retrieval. Q.J.R.M.S. , 2854–2866doi:https://doi.org/10.1002/qj.2873.

Bell, W., English, S.J., Candy, B., Atkinson, N., Hilton, F., Baker, N., Swadley, S.D., Campbell, W.F., Bormann, N., Kelly, G., Kazumori, M., 2008. The Assimilation of SSMIS Radiances in Numerical Weather Prediction models. IEEE Transactions on Geoscience and Remote Sensing 46, 884–900. doi:10.1109/TGRS.2008.917335.

Bennartz, R., Thoss, A., Dybbroe, A., Michelson, D., 2002. Precipitation analysis using the Advanced Microwave Sounding Unit in support of nowcasting applications. Met. Apps , 177–189doi:https://doi.org/10.1017/S1350482702002037.

Bonavita, M., Isaksen, L., Holm, E., 2012. On the use of EDA background error variances in the ECMWF 4D-Var. Quart. J. Roy. Meteorol. Soc 138, 1540–1559.

Bonavita, M., Raynaud, L., Isaksen, L., 2011. Estimating background-error variances with the ECMWF Ensemble of Data Assimilations system: some effects of ensemble size and day-to-day variability. Quart. J. Roy. Meteorol. Soc. , 423–434.

Bormann, N., 2017. Slant path radiative transfer for the assimilation of sounder radiances. Tellus A: Dynamic Meteorology and Oceanography 69, 1272779. doi:10.1080/16000870.2016.1272779.

Bormann, N., Fouilloux, A., Bell, W., 2013. Evaluation and assimilation of atms data in the ecmwf system. Journal of Geophysical Research: Atmospheres , 12,970–12,980doi:https://doi.org/10.1002/2013JD020325.

Bormann, N., Lawrence, H., Farnan, J., 2019. Global observing system experiments in the ECMWF assimilation system. ECMWF Technical Memorandum No.839.

Cardinali, C., Žagar, N., Radnoti, G., Buizza, R., 2014. Representing model error in ensemble data assimilation. ECMWF Technical Memorandum .

Coordination Group for Meteorological Satellites, 2022. CGMS Baseline: Sustained contributions to the observing of the Earth system, space environment and the Sun. Available online at https://cgms-info.org/publication/cgms-baseline/ (Accessed 1 Aug 2022) CGMS/DOC/18/1028862, v.4.

Desroziers, G., Berre, L., Chapnik, B., Poli, P., 2005. Diagnosis of observation, background, and analysis-error statistics in observation space. Q. J. R. Meteorol. Soc. 131, 3385–3396.

Dirksen, R.J., Sommer, M., Immler, F.J., Hurst, D.F., Kivi, K., V omel, H., 2014. Reference quality upper-air measurements: GRUAN data processing for the Vaisala RS92 radiosonde. Atmos. Meas. Tech. 7, 4463–4490.

Duncan, D.I., Bormann, N., 2020. On the Addition of Microwave Sounders and NWP Skill, Including Assessment of FY-3D Sounders. EUMETSAT/ECMWF Fellowship Programme Research Report No.55.

Duncan, D.I., Bormann, N., Geer, A.J., Weston, P., 2022. Assimilation of AMSU-A in All-Sky Conditions. Monthly Weather Review 150, 1023 – 1041. doi:10.1175/MWR-D-21-0273.1.

Duncan, D.I., Bormann, N., Hólm, E.V., 2021. On the addition of microwave sounders and numerical weather prediction skill. Q. J. R. Meteorol. Soc. 147, 3703–3718. doi:https://doi.org/10.1002/qj.4149.

Geer, A., Baordo, F., Bormann, N., Chambon, P., English, S., Kazumori, M., Lawrence, H., Lean, P., Lonitz, K., Lupu, C., 2017. The growing impact of satellite observations sensitive to humidity, cloud and precipitation. Q.J.R. Meteorol. Soc. 143, 3189–3206. doi:doi:10.1002/qj.3172.

Geer, A., Baordo, F., Bormann, N., English, S., 2014. All-sky assimilation of microwave humidity sounders. ECMWF Technical Memorandum No. 741, 57pp.

Geer, A., Bauer, P., Lopez, P., 2010. Direct 4D-Var assimilation of all-sky radiances. Part II: Assessment. ECMWF Technical Memorandum No.619.

Geer, A.J., 2021. Physical characteristics of frozen hydrometeors inferred with parameter estimation. Atmospheric Measurement Techniques 14, 5369–5395. URL: https://amt.copernicus.org/articles/14/5369/2021/, doi:10.5194/amt-14-5369-2021.

Geer, A.J., Baordo, F., 2014. Improved scattering radiative transfer for frozen hydrometeors at microwave frequencies. Atmos. Meas. Tech. 7, 1839–1860.

Geer, A.J., Bauer, P., 2011. Observation errors in all-sky data assimilation. Q. J. R. Meteorol. Soc. 137, 2024–2037. doi:doi:10.1002/qj.830.

Geer, A.J., Bauer, P., Lonitz, K., Barlakas, V., Eriksson, P., Mendrok, J., A. Doherty, J.H., Chambon, P., 2021. Bulk hydrometeor optical properties for microwave and sub-millimetre radiative transfer in RTTOV-SCATT v13.0. Geosci Model Dev 14, 7497–7526. doi:10.5194/gmd-14-7497-2021.

Geer, A.J., Lonitz, K., Duncan, D., Bormann, N., 2022. Improved surface treatment for all-sky microwave observations. ECMWF Technical Memoranda URL: https://www.ecmwf.int/node/20337, doi:10.21957/zi7q6hau.

Grody, N., Zhao, J., Ferraro, R., Weng, F., , Boers, R., 2001. Determination of precipitable water and cloud liquid water over oceans from the NOAA 15 advanced microwave sounding unit. J. Geophys. Res. , 2943–2953doi:doi:10.1029/2000JD900616.

Harnisch, F., Healy, S.B., Bauer, P., English, S.J., 2013. Scaling of GNSS Radio Occultation Impact with Observation Number Using an Ensemble of Data Assimilations. Mon. Wea. Rev. 141, 4395–4413. doi:doi:http://dx.doi.org/10.1175/MWRD-13-00098.1.

Ingleby, B., 2017. An assessment of different radiosonde types 2015/2016. ECMWF Technical Memorandum No.807.

Isaksen, L., Bonavita, M., Buizza, R., Fisher, M., Haseler, J., Leutbecher, M., Raynaud, L., 2010. Ensemble of data assimilations at ECMWF. ECMWF Technical Memorandum No.636, pp. 45. URL: https://www.ecmwf.int/node/10125, doi:10.21957/obke4k60.

JCR Systems, 2022. Input Generation for Study to Assess Earth Observation with Small Satellites and their Prospects for Future Global Numerical Weather Prediction (SSat4-GNWP). ESA Contract No: 400013468, Final Report (unpublished) .

Karbou, F., Gérard, E., Rabier, F., 2006. Microwave land emissivity and skin temperature for AMSU-A and -B assimilation over land. QJRMS 132, 2333–2355.

Kazumori, M., English, S.J., 2015. Use of the ocean surface wind direction signal in microwave radiance assimilation. QJRMS 141, 1354–1375. URL: https://rmets.onlinelibrary.wiley.com/doi/abs/10.1002/qj.2445, doi:doi:10.1002/qj.2445.

Lagaune, B., Sten, B., Emrich, A., 2021. Arctic Weather Satellite, A microsatellite constellation for improved weather forecasting in Arctic and globally. Proceedings of the AIAA/USU Conference on Small Satellites, Mission Lessons, SSC21-XII-02, Logan, Utah, U.S.A. URL: http://digitalcommons.usu.edu/smallsat/2021/all2021/213/.

Lean, K., Bormann, N., Healy, S., 2021a. Technical Note 1 for ESA Contract No. ESA 4000130590/20/NL/IA: WP-1000 Review of EDA approach and recommendations for small satellite configurations. ESA Contract 4000130590/20/NL/IA Technical Note 1 URL: https://www.ecmwf.int/node/20304, doi:10.21957/osvhislk.

Lean, K., Bormann, N., Healy, S., 2021b. Technical Note 2 for ESA Contract No. ESA 4000130590/20/NL/IA: WP-2000 Calibration of EDA spread and adaptation of the observation error model. ESA Contract 4000130590/20/NL/IA Technical Note 2 URL: https://www.ecmwf.int/node/20302, doi:10.21957/1auh0nztg.

Lean, K., Bormann, N., Healy, S., 2022. Technical Note 3 for ESA Contract No. ESA 4000130590/20/NL/IA: WP-3000. ESA Contract 4000130590/20/NL/IA Technical Note 3 URL: https://www.ecmwf.int/node/20303, doi:10.21957/kjmxyh9xy.

Lonitz, K., Marquardt, C., Bowler, N., Healy, S., 2021. Final Technical Note of Impact assessment of commercial GNSS-RO data. ESA contract 4000131086/20/NL/FF/a Final Report URL: https://www.ecmwf.int/node/20240, doi:10.21957/wrh6voyyi.

Lui, G., 2008. A database of microwave single-scattering properties for nonspherical ice particles. Bull. Am. Met. Soc. , 1563–1570.

Masutani, M., Andersson, E., Terry, J., Reale, O., Jusem, J., Riishøjgaard, L., Schlatter, T., Stoffelen, A., Woollen, J., Lord, S., Tóth, Z., Song, Y., Kleist, D., Xie, Y., Prive, N., Liu, E., Sun, H., Emmitt, D., Boukabara, S.A., 2007. Progress in joint osses a new nature run and international collaboration. AMS preprint volume for 18th conference on Numerical Weather Prediction, Parkcity, Utah. 25 - 29 June 2007 .

Masutani, M., Schlatter, T., Errico, R., Stoffelen, A., Andersson, E., Lahoz, W., Woollen, J., Emmitt, G., Riishøjgaard, L.P., Lord, S., 2010. Data Assimilation: Making sense of observations, Observing System Simulation Experiments. Eds. W.A. Lahoz, B. Khattatov and R. Ménard, Springer , 647–679.

Palmer, T., Buizza, R., Doblas-Reyes, F., Jung, T., Leutbecher, M., Shutts, G., Steinheimer, M., Weisheimer, A., 2009. Stochastic parametrization and model uncertainty. ECMWF Technical Memorandum , 42.

Saunders, R., Hocking, J., Turner, E., Havemann, S., Geer, A., Lupu, C., Vidot, J., Chambon, P., Köpken-Watts, C., Scheck, L., Stiller, O., Stumpf, C., Borbas, E., 2020. RTTOV-13 science and validation report. EUMETSAT NWP SAF, version 1.0 URL: https://nwp-saf.eumetsat.int/site/software/rttov/documentation/.

Tan, D.G.H., Andersson, E., Fisher, M., Isaksen, L., 2007. Observing-system impact assessment using a data assimilation ensemble technique: Application to the ADM-Aeolus wind profiling mission. Quart. J. Roy. Meteor. Soc. 133, 381–390.

World Meteorological Organisation, 2019. Vision for the WMO Integrated Global Observing System in 2040 WMO- No. 1243.